Supporting information for an allosteric theory of transcription factor induction

Manuel Razo-Mejia[1,†]**, Stephanie L. Barnes**[1,†]**, Nathan M. Belliveau**[1,†]**, Griffin Chure**[1,†]**, Tal Einav**[2,†]**, Rob Phillips**[1,3,*]

[1]Division of Biology and Biological Engineering, California Institute of Technology, Pasadena, United States; [2]Department of Physics, California Institute of Technology, Pasadena, United States; [3]Department of Applied Physics, California Institute of Technology, Pasadena, United States

[†] contributed equally

[*] phillips@pboc.caltech.edu

Contents

A The Lac Repressor: Two Independent Allosteric Dimers vs An Allosteric Tetramer

In this work, we have been concerned with the allosteric nature of the Lac repressor. As stated in the main text, the Lac repressor is comprised of two identical dimers, with each dimer containing one DNA binding domain and two inducer binding sites. Although the Lac repressor is known to be allosteric, to our knowledge the exact nature of the allostery between the two Lac dimers has not been fully characterized. In this section, we consider two different mechanisms of allostery for the Lac repressor. The first model assumes that each dimer is allosterically independent, so that the two dimers within a single Lac repressor can be in the active/active, active/inactive, inactive/active, or inactive/inactive states (this is the model that we used in the main text). The second model assumes that the allostery of the Lac repressor is shared between both dimers, so that the two dimers within a single Lac repressor can only be either active/active or inactive/inactive.

We show how both models can characterize the induction curves given in Fig. 5 of the main text (albeit for different value of the physical parameters). We then show that the two models make vastly different predictions for the induction profiles of the Lac repressor whose tetramerization region has been removed, thereby providing a possible means to experimentally distinguish between the two models.

A.1 Two Independent Allosteric Dimers

First, we assume that the two dimers in a Lac repressor are allosterically independent, so that the allosteric conformation of one dimer does not affect the allosteric conformation of the other dimer. Fig. 2 in the main text shows the possible states and weights for either Lac repressor dimer in this case. Considering only one of the two Lac dimers in a given tetramer, the probability that this dimer is in the active state is given by

$$p_A^{\text{dimer}}(c) = \frac{\left(1 + \frac{c}{K_A}\right)^2}{\left(1 + \frac{c}{K_A}\right)^2 + e^{-\beta \Delta \varepsilon_{AI}} \left(1 + \frac{c}{K_I}\right)^2}. \tag{S1}$$

As in the main text R represents the copy number of Lac repressor dimers (i.e. twice the copy number of Lac repressors per cell, since a Lac repressor is comprised of two dimers). Substituting $p_A^{\text{dimer}}(c)$ into Eq. (3) yields the same formula for fold-change Eq. (5) given in the main text, namely,

$$\text{fold-change} = \left(1 + \frac{\left(1 + \frac{c}{K_A}\right)^2}{\left(1 + \frac{c}{K_A}\right)^2 + e^{-\beta \Delta \varepsilon_{AI}} \left(1 + \frac{c}{K_I}\right)^2} \frac{R}{N_{NS}} e^{-\beta \Delta \varepsilon_{RA}}\right)^{-1}. \tag{S2}$$

Following the main text, we use the allosteric energy $\Delta \varepsilon_{AI} = 4.5 \ k_B T$ (see Appendix D) and fit the single O2 strain ($\Delta \varepsilon_{RA} = -13.9 \ k_B T$) with $R = 260$ repressors/cell to obtain the physical parameters $K_A = 196^{+11}_{-11} \times 10^{-6}$ M and $K_I = 0.63^{+0.02}_{-0.02} \times 10^{-6}$ M. We can then use these parameters to predict the response at other repressor copy numbers and DNA binding energies, as shown Fig. S1A.

We note that unlike in the main text, here we are simultaneously fitting data from all the strains to get the best estimate of the K_A and K_I values. By fitting the entire data set, we can compare how well the two theories - that the Lac repressor is comprised of two independent dimers versus an allosteric tetramer - can characterize the data.

A.2 An Allosteric Tetramer

We now turn to a second model of the Lac tetramer, where the two Lac repressor dimers must either be simultaneously active or simultaneously inactive. In other words, the repressor as a whole is either active or inactive. In such a case, the Lac repressor can be viewed as an allosteric receptor with four identical
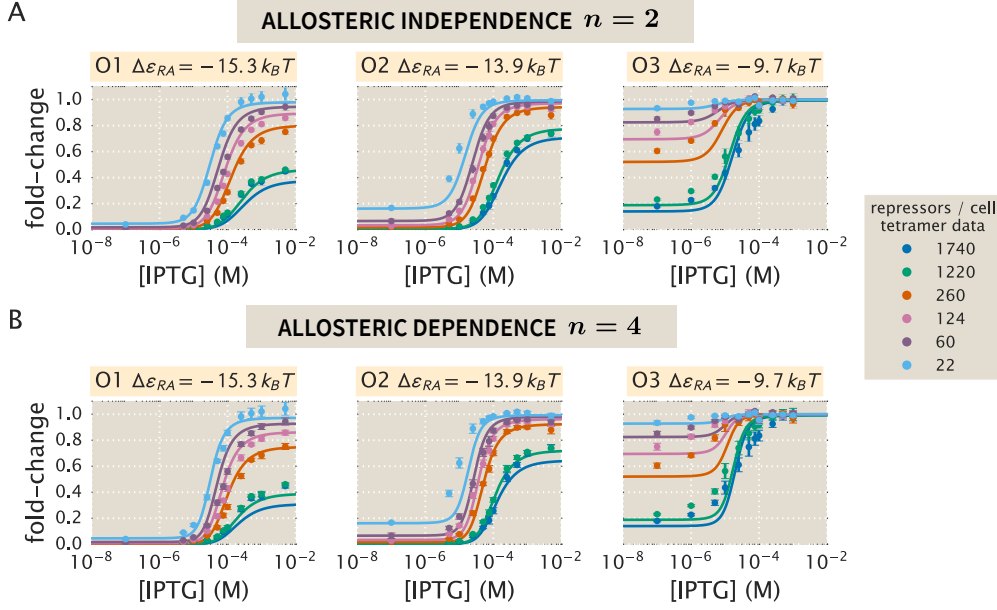
Figure S1. Two models of allostery for the Lac repressor. (A) The induction profiles assuming that a Lac repressor is comprised of two allosterically independent dimers using Eq. (S2). Fitting the entire data set yields the best-fit parameters $K_A = 196^{+11}_{-11} \times 10^{-6}$ M and $K_I = 0.63^{+0.02}_{-0.02} \times 10^{-6}$ M. (B) If the Lac repressor is an allosteric tetramer, the induction profile is given by Eq. (S4). Fitting the entire data set yields the different set of parameters $K_A = 57^{+3}_{-3} \times 10^{-6}$ M and $K_I = 3.5^{+0.1}_{-0.1} \times 10^{-6}$ M. Note that while the $n = 4$ curves are slightly sharper, they closely match the $n = 2$ curves.

inducer binding sites, which implies that the probability that the Lac repressor is active is given by

$$p_A^{\text{tetramer}}(c) = \frac{\left(1 + \frac{c}{K_A}\right)^4}{\left(1 + \frac{c}{K_A}\right)^4 + e^{-\beta \Delta \varepsilon_{AI}} \left(1 + \frac{c}{K_I}\right)^4}. \tag{S3}$$

Substituting $p_A^{\text{tetramer}}(c)$ into Eq. (3) yields a fold-change whose exponents are fourth powers,

$$\text{fold-change} = \left(1 + \frac{\left(1 + \frac{c}{K_A}\right)^4}{\left(1 + \frac{c}{K_A}\right)^4 + e^{-\beta \Delta \varepsilon_{AI}} \left(1 + \frac{c}{K_I}\right)^4} \frac{R}{N_{NS}} e^{-\beta \Delta \varepsilon_{RA}}\right)^{-1}, \tag{S4}$$

reflecting the fact that all four inducer binding sites influence the single allosteric state of the Lac repressor. Note that the factor of R appears because there are $R/2$ Lac repressors per cell, but each one is able to bind to the operator in two ways (i.e. with each dimer).

As in the previous case, we use the allosteric energy $\Delta \varepsilon_{AI} = 4.5 \, k_B T$ (see Appendix D) and fit the single O2 strain ($\Delta \varepsilon_{RA} = -13.9 \, k_B T$) with $R = 260$ repressors/cell to obtain the physical parameters $K_A = 57^{+2}_{-3} \times 10^{-6}$ M and $K_I = 3.5^{+0.1}_{-0.1} \times 10^{-6}$ M . We can then predict the induction profiles at other repressor copy numbers and DNA binding energies and compare these predictions to experimental data, as shown in Fig. S1B. Again, we note that these are global fits using all of the data.
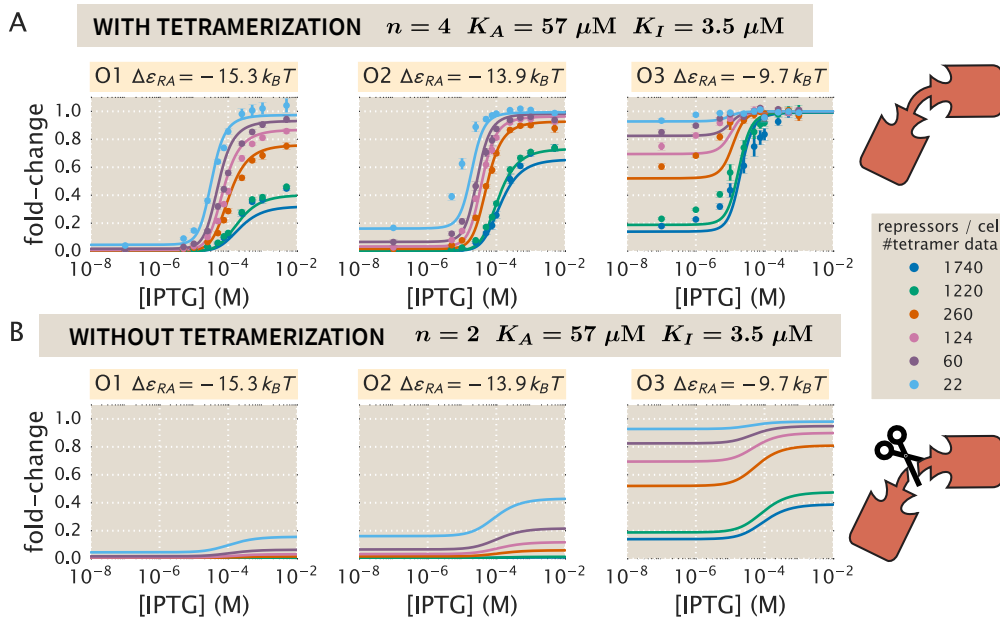
A.3 Removing the Tetramerization Region

The above two sections demonstrate that the two modes of allostery can both be used to characterize the induction data in Fig. 5, although they predict different values for the physical parameters K_A and K_I. In this section, we propose an experiment that may differentiate between these two models of allostery.

It has been shown that removing the tetramerization region in the *lac* gene results in a functional dimeric repressor that: (1) can bind to DNA; (2) exists in both an active and inactive allosteric conformation; and (3) has two binding sites for the inducer IPTG [1–4]. We now consider what the induction profile of such a construct would look like.

For the first model considered above where the Lac repressor consists of two independent allosteric dimers, cutting the tetramerization region should have no effect on the Lac repressor. This dimeric Lac repressor would have the same states and weights shown in Fig. 2, so that its probability of being active is still given by Eq. (S1) and the fold-change equation would still be given by Eq. (S2). Therefore, the predicted induction curves are identical to those shown in Fig. S1A. Note that this analysis assumes that removing the tetramerization region does not alter the thermodynamic parameter K_A, K_I, and $\Delta\varepsilon_{AI}$.

On the other hand, within the second model of allostery where the Lac repressor is an allosteric tetramer, removing the tetramerization region would have a large effect on the induction profiles. But now each dimer must necessarily be active or inactive independently of all other dimers, and therefore the probability of a repressor being active and the corresponding equation fold-change would change from the tetramer version Eq. (S4) to the dimer version Eq. (S2). This shift in the exponents from fourth powers to second powers dramatically changes the fold-change curves. Fig. S2 demonstrates that indeed the induction profiles for the O1, O2, and O3 strains are predicted to significantly decrease after the tetramerization region of the Lac repressor has been removed. Therefore, this experimental measurement could be done to differentiate these two models of allostery within the Lac repressor.

Figure S2. Removing the tetramerization region of the Lac repressor. (A) The same data and best-fit curves from Fig. S1A assuming that the Lac repressor is an allosteric tetramer. (B) Upon removing the tetramerization region, the induction profile of the repressor will significantly change from Eq. (S4) to Eq. (S2). If data from a dimer experiment would match data from a tetramer experiment, it would support the hypothesis that the Lac repressor is comprised of two allosterically independent dimers; conversely, significant discrepancies between these two data sets would support the allosteric tetramer model. Note that analysis assumes that removing the tetramerization region does not alter the thermodynamic parameter K_A, K_I, and $\Delta\varepsilon_{AI}$.

B Flow Cytometry

In this section, we provide information regarding the equipment used to make experimental measurements of the fold-change in gene expression in the interests of transparency and reproducibility. We also provide a summary of our unsupervised method of gating the flow cytometry measurements for consistency between experimental runs.

B.1 Equipment

Due to past experience using the Miltenyi Biotec MACSQuant flow cytometer during the Physiology summer course at the Marine Biological Laboratory, we used the same flow cytometer for the formal measurements in this work. All measurements were made using an excitation wavelength of 488 nm with an emission filter set of 520/50 nm. This excitation wavelength provides approximately 40% of the maximum YFP absorbance [5], and this was found to be sufficient for the purposes of this experiment. A useful feature of modern flow cytometry is the high-sensitivity signal detection through the use of photomultiplier tubes (PMT) whose response can be tuned by adjusting the voltage. Thus, the voltage for the forward-scatter (FSC), side-scatter (SSC), and gene expression measurements were tuned manually to maximize the dynamic range between autofluorescence signal and maximal expression without losing the details of the population distribution. Once these voltages were determined, they were used for all subsequent measurements. Extremely low signal producing particles were discarded before data storage by setting a basal voltage threshold, thus removing the majority of spurious events. The various instrument settings for data collection are given in Table S1.

Table S1. Instrument settings for data collection using the Miltenyi-Biotec MACSQuant flow cytometer. All experimental measurements were collected using these values.

Laser	Channel	Sensor Voltage
488 nm	Forward-Scatter (FSC)	423 V
488 nm	Side-Scatter (SSC)	537 V
488 nm	Intensity (B1 Filter, 525/50nm)	790 V
488 nm	Trigger (debris threshold)	24.5 V

B.2 Experimental Measurement

Collection of a single data set consisting of all eight bacterial strains under twelve IPTG concentrations took place over two to three hours. During this time, the cultures were held at approximately 4°C by placing the 96-well plate on a MACSQuant ice block. Because the ice block thawed over the course of the experiment, the samples measured last were approximately at room temperature. This means that samples may have grown slightly by the end of the experiment. To confirm that this continued growth did not alter the measured results, a subset of experiments were run in reverse meaning that the fully induced cultures were measured first and the uninduced samples last. The plate arrangements and corresponding fold-change measurements are shown in Fig. S3A and Fig. S3B, respectively. The measured fold-change values in the reverse ordered plate appear to be drawn from the same distribution as those measured in the forward order, meaning that any growth that might have taken place during the experiment did not significantly affect the results. Both the forward and reverse data sets were used in our analysis.

B.3 Unsupervised Gating

As explained in the Methods, we used an automatic unsupervised gating procedure to filter the flow cytometry data based on the front and side-scattering values returned by the MACSQuant flow cytometer. We assume that the region with highest density of points in these two channels corresponds to single-cell
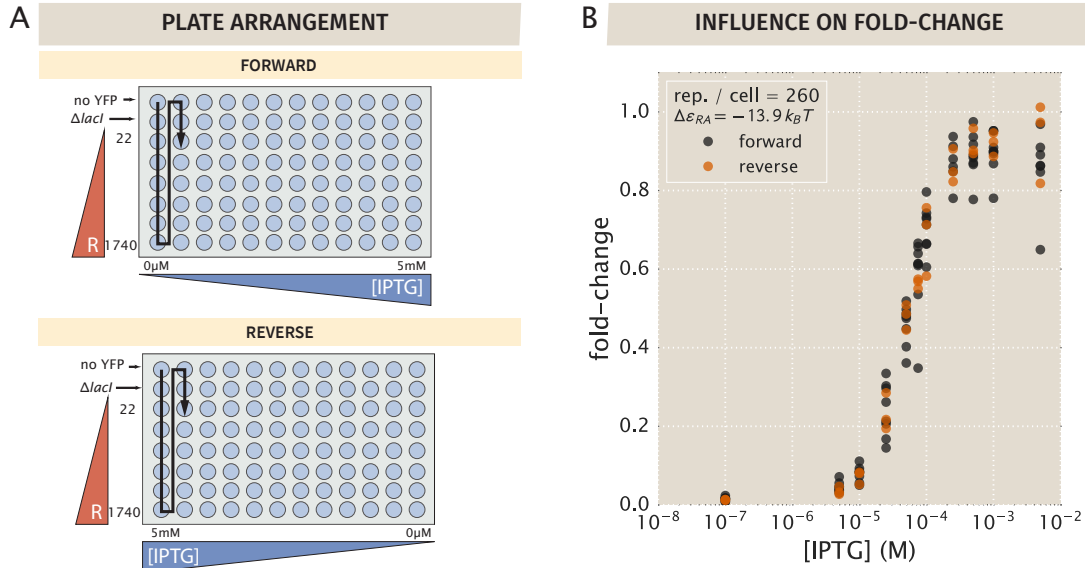
Figure S3. Plate arrangements for flow cytometry. (A) Samples were measured primarily in the forward arrangement with a subset of samples measured in reverse. The black arrow indicates the order in which samples were processed by the flow cytometer. (B) The experimentally measured fold-change values for the two sets of plate arrangements show that samples measured in the reverse arrangement appear to be indistinguishable from those measured in reverse order.

measurements. Everything extending outside of this region was discarded in order to exclude sources of error such as cell clustering, particulates, or other spurious events.

In order to define the gated region we fit a two-dimensional Gaussian function to the $\log_{10}$ forward scattering (FSC) and the $\log_{10}$ side scattering (SSC) data. We then kept a fraction $\alpha \in [0, 1]$ of the data by defining an elliptical region given by

$$(\boldsymbol{x} - \boldsymbol{\mu})^T \boldsymbol{\Sigma}^{-1} (\boldsymbol{x} - \boldsymbol{\mu}) \leq \chi_\alpha^2(p), \; , \tag{S5}$$

where $\boldsymbol{x}$ is the 2×1 vector containing the log FSC and log SSC, $\boldsymbol{\mu}$ is the 2×1 vector representing the mean values of log FSC and log SSC as obtained from fitting a two-dimensional Gaussian to the data, and $\boldsymbol{\Sigma}$ is the 2×2 covariance matrix also obtained from the Gaussian fit. $\chi_\alpha^2(p)$ is the quantile function for probability p of the chi-squared distribution with two degrees of freedom. Fig. S4 shows an example of different gating contours that would arise from different values of α in Eq. (S5). In this work, we chose $\alpha = 0.4$ which we deemed was a sufficient constraint to minimize the noise in the data. As explained in Appendix C we compared our high throughput flow cytometry data with single cell microscopy, confirming that the automatic gating did not introduce systematic biases to the analysis pipeline. The specific code where this gating is implemented can be found in GitHub repository.

B.4   Comparison of Flow Cytometry with Other Methods

Previous work from our lab experimentally determined fold-change for similar simple repression constructs using a variety of different measurement methods [6,7]. Garcia and Phillips used the same background strains as the ones used in this work, but gene expression was measured with Miller assays based on colorimetric enzymatic reactions with the LacZ protein [8]. Brewster *et al.* used a LacI dimer with the tetramerization replaced with an mCherry tag. In this case the fold-change was measured as the ratio of the gene expression rate rather than a single snapshot [7].

Fig. S5 shows the comparison of these methods along with the flow cytometry method used in this work. The consistency of these three readouts validates the quantitative use of flow cytometry and unsupervised gating to determine the fold-change in gene expression. However, one important
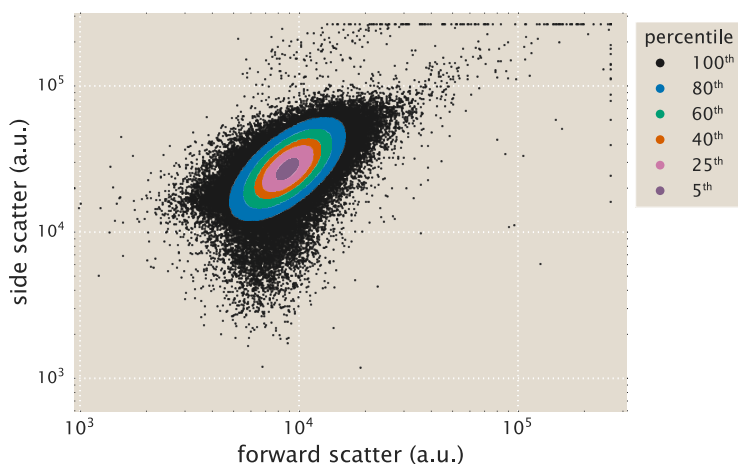
Figure S4. Representative unsupervised gating contours. Points indicate individual flow cytometry measurements of forward scatter and side scatter. Colored points indicate arbitrary gating contours ranging from 100% ($\alpha = 1.0$) to 5% ($\alpha = 0.05$). All measurements for this work were made computing the mean fluorescence from the 40$^{\text{th}}$ percentile ($\alpha = 0.4$), shown as orange points.

caveat revealed by this figure is that the sensitivity of flow cytometer measurements is not sufficient to accurately determine the fold-change for the high repressor copy number strains in O1 without induction. Instead, a method with a large dynamic range such as the Miller assay is needed to accurately resolve the fold-change of such low expression levels.
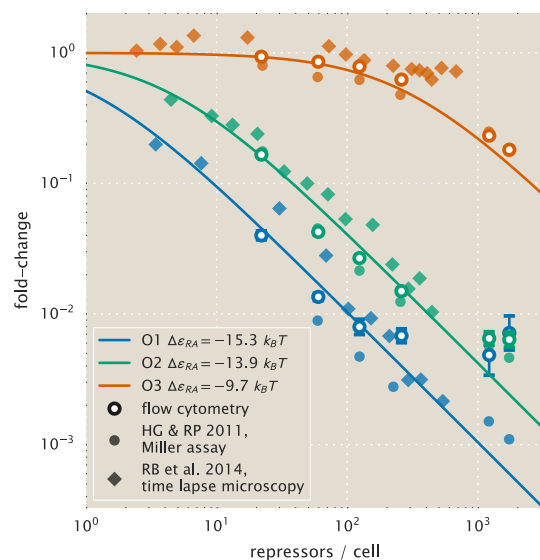
Figure S5. Comparison of experimental methods to determine the fold-change. The fold-change in gene expression for equivalent simple-repression constructs has been determined using three independent methods: flow cytometry (this work), colorimetric Miller assays [8], and time lapse microscopy [7]. All three methods give consistent results, although flow cytometry measurements lose accuracy for fold-change less than 10^{-2}. Note that the repressor-DNA binding energies $\Delta\varepsilon_{RA}$ used for the theoretical predictions were determined in [8].

C   Single-Cell Microscopy

In this section, we detail the procedures and results from single-cell microscopy verification of our flow cytometry measurements. Our previous measurements of fold-change in gene expression have been measured using bulk-scale Miller assays [8] or through single-cell microscopy [7]. In this work, flow cytometry was an attractive method due to the ability to screen through many different strains at different concentrations of inducer in a short amount of time. To verify our results from flow cytometry, we examined two bacterial strains with different repressor-DNA binding energies ($\Delta\varepsilon_{RA}$) of $-13.9\ k_BT$ and $-15.3\ k_BT$ with 260 repressors per cell using fluorescence microscopy and estimated the parameter values for direct comparison between the two methods. For a detailed explanation of the Python code implementation of the processing steps described below, please see this paper's GitHub repository. An outline of our microscopy workflow can be seen in Fig. S6.

C.1   Strains and Growth Conditions

Cells were grown in an identical manner to those used for measurement via flow cytometry (see Materials and Methods, main text). Briefly, cells were grown overnight (between 10 and 13 hours) to saturation in rich media broth (LB) with $100\,\mu\text{g}\cdot\text{mL}^{-1}$ spectinomycin in a deep-well 96 well plate at 37°C. These cultures were then diluted 1000 fold into $500\,\mu$L of M9 minimal medium supplemented with 0.5% glucose and the appropriate concentration of the inducer IPTG. Strains were allowed to grow at 37°C with vigorous aeration for approximately 8 hours. Prior to mounting for microscopy, the cultures were diluted ten fold into M9 glucose minimal medium in the absence of IPTG.

For the purposes of comparison, we examined only one repressor copy number ($R = 260$) with two different repressor binding energies $\Delta\varepsilon_{RA} = -13.9\ k_BT$ and $\Delta\varepsilon_{RA} = -15.3\ k_BT$ [8]. Each construct was measured using the same range of inducer concentration values as was performed in the flow cytometry measurements (between $100\,$nM and $5\,$mM IPTG). Each condition was measured in triplicate in microscopy whereas approximately ten measurements were made using flow cytometry.

C.2   Imaging Procedure

During the last hour of cell growth, an agarose mounting substrate was prepared containing the appropriate concentration of the IPTG inducer. This mounting substrate was composed of M9 minimal medium supplemented with 0.5% glucose and 2% agarose (Life Technologies UltraPure Agarose, Cat. No. 16500100). This solution was heated in a microwave until molten followed by addition of the IPTG to the appropriate final concentration. This solution was then thoroughly mixed and a $500\ \mu$L aliquot was sandwiched between two glass coverslips and was allowed to solidify.

Once solid, the agarose substrates were cut into approximately $10\,$mm $\times\,10\,$mm squares. An aliquot of one to two microliters of the diluted cell suspension was then added to each pad. For each concentration of inducer, a sample of the autofluorescent control, the $\Delta lacI$ constitutive expression control, and the experimental strain was prepared yielding a total of thirty-six agarose mounts per experiment. These samples were then mounted onto two glass-bottom dishes (Ted Pella Wilco Dish, Cat. No. 14027-20) and sealed with parafilm.

All imaging was performed on a Nikon Ti-Eclipse inverted fluorescent microscope outfitted with a custom built laser illumination system and operated by the open-source MicroManager control software [9]. The YFP fluorescence was imaged using a CrystaLaser $514\,$nm excitation laser coupled with a laser-optimized (Semrock Cat. No. LF514-C-000) emission filter.

For each sample, between fifteen and twenty positions were imaged allowing for measurement of several hundred cells. At each position, a phase contrast image, an mCherry image, and a YFP image were collected in that order with exposures on a time scale of ten to twenty milliseconds. For each channel, the same exposure time was used across all samples in a given experiment. All images were collected and stored in `ome.tiff` format. All microscopy images are available upon request.
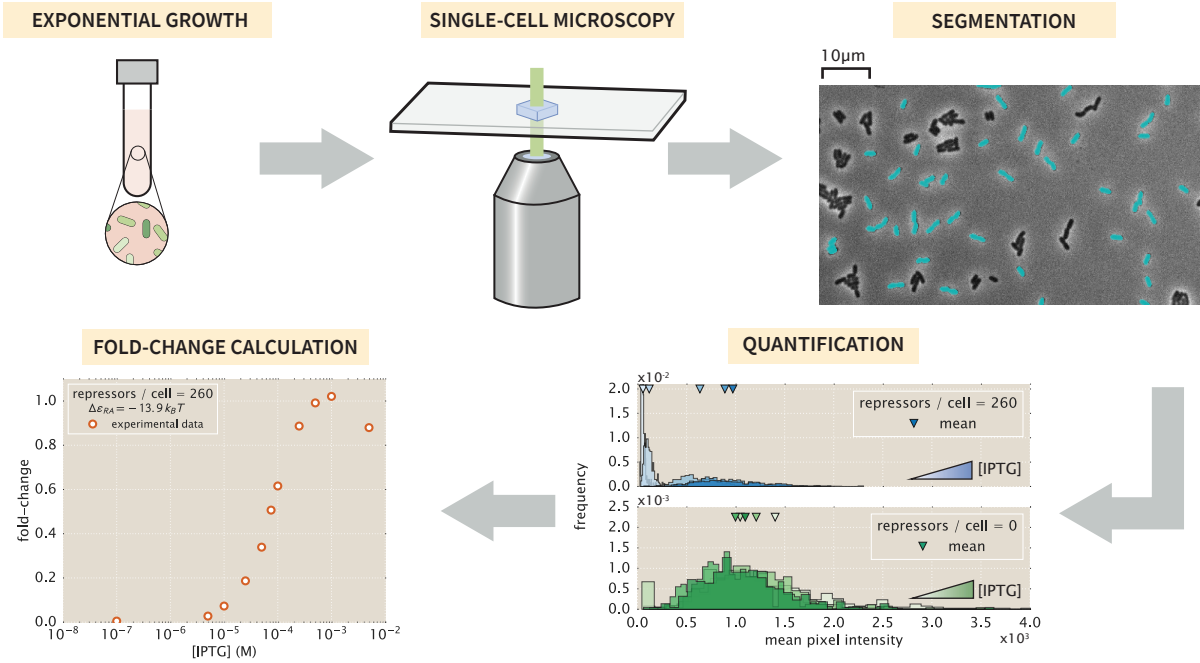
Figure S6. Experimental workflow for single-cell microscopy. For comparison with the flow cytometry results, the cells were grown in an identical manner to those described in the main text. Once cells had reached mid to late exponential growth, the cultures were diluted and placed on agarose substrates and imaged under $100\times$ magnification. Regions of interest representing cellular mass were segmented and average single-cell intensities were computed. The mean of the distributions were used to compute the fold-change in gene expression.

C.3   Image Processing

C.3.1   Correcting Uneven Illumination

The excitation laser has a two-dimensional gaussian profile. To minimize non-uniform illumination of a single field of view, the excitation beam was expanded to illuminate an area larger than that of the camera sensor. While this allowed for an entire field of view to be illuminated, there was still approximately a 10% difference in illumination across both dimensions. This nonuniformity was corrected for in post by capturing twenty images of a homogenously fluorescent plastic slide (Autofluorescent Plastic Slides, Chroma Cat. No. 920001) and averaging to generate a map of illumination intensity at any pixel I_{YFP}. To correct for shot noise in the camera (Andor iXon+ 897 EMCCD), twenty images were captured in the absence of illumination using the exposure time used for the experimental data. Averaging over these images produced a map of background noise at any pixel I_{dark}. To perform the correction, each fluorescent image in the experimental acquisition was renormalized with respect to these average maps as

$$I_{\mathrm{flat}} = \frac{I - I_{\mathrm{dark}}}{I_{\mathrm{YFP}} - I_{\mathrm{dark}}} \langle I_{\mathrm{YFP}} - I_{\mathrm{dark}} \rangle, \tag{S6}$$

where I_{flat} is the renormalized image and I is the original fluorescence image. An example of this correction can be seen in Fig. S7.

C.3.2   Cell Segmentation

Each bacterial strain constitutively expressed an mCherry fluorophore from a low copy-number plasmid. This served as a volume marker of cell mass allowing us to segment individual cells through edge detection in fluorescence. We used the Marr-Hildreth edge detector [10] which identifies edges by taking the second
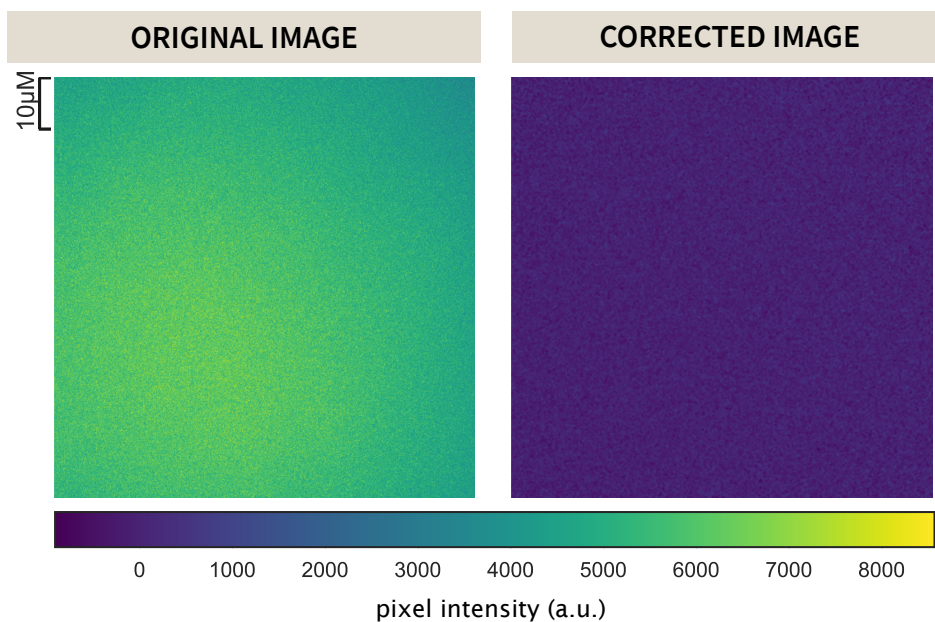
Figure S7. Correction for uneven illumination. A representative image of the illumination profile of the 512 nm excitation beam on a homogenously fluorescent slide is shown in the left panel. This is corrected for using equation Eq. (S6) and is shown in the right panel.

derivative of a lightly Gaussian blurred image. Edges are identified as those regions which cross from highly negative to highly positive values or vice-versa within a specified neighborhood. Bacterial cells were defined as regions within an intact and closed identified edge. All segmented objects were then labeled and passed through a series of filtering steps.

To ensure that primarily single cells were segmented, we imposed area and eccentricity bounds. We assumed that single cells projected into two dimensions are roughly $2\,\mu$m long and $1\,\mu$m wide, so that cells are likely to have an area between $0.5\,\mu$m^2 and $6\,\mu$m. To determine the eccentricity bounds, we assumed that the a single cell can be approximated by an ellipse with semimajor (a) and semiminor (b) axis lengths of $0.5\,\mu$m and $0.25\,\mu$m respectively. The eccentricity of this hypothetical cell can be computed as

$$\text{eccentricity} = \sqrt{1 - \left(\frac{b}{a}\right)^2}, \tag{S7}$$

yielding a value of approximately 0.8. Any objects with an eccentricity below this value were not considered to be single cells. After imposing both an area (Fig. S8A) and eccentricity filter (Fig. S8B), the remaining objects were considered cells of interest (Fig. S8C) and the mean fluorescence intensity of each cell was extracted.

C.3.3 Calculation of Fold-Change

Cells exhibited background fluorescence even in the absence of an expressed fluorophore. We corrected for this autofluorescence contribution to the fold-change calculation by subtracting the mean YFP fluorescence of cells expressing only the mCherry volume marker from each experimental measurement. The fold-change in gene expression was therefore calculated as

$$\text{fold-change} = \frac{\langle I_{R>0} \rangle - \langle I_{\text{auto}} \rangle}{\langle I_{R\,=\,0} \rangle - \langle I_{\text{auto}} \rangle}, \tag{S8}$$

S11
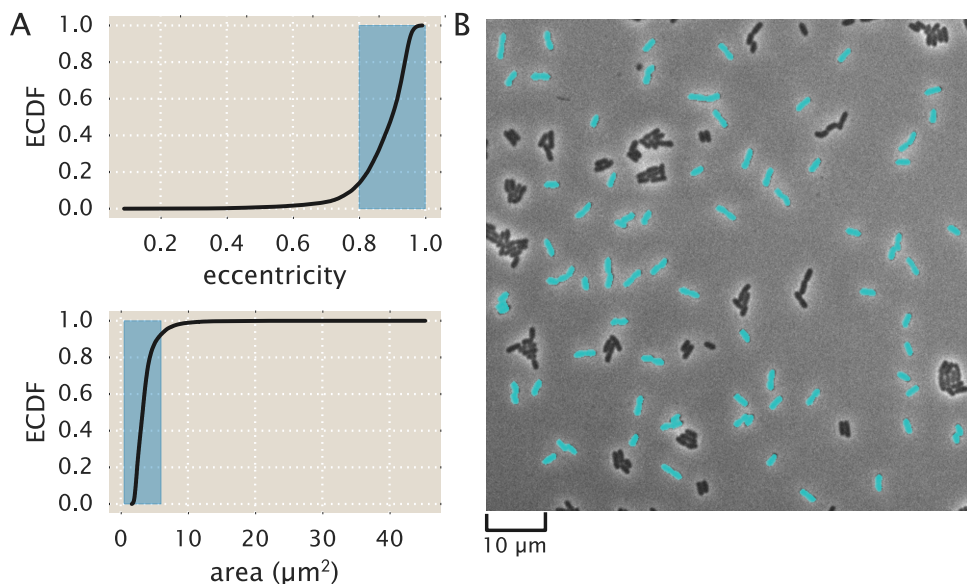
Figure S8. Segmentation of single bacterial cells. (A) Objects with an area between $0.5\,\mu\mathrm{m}^2$ and $6\,\mu\mathrm{m}^2$ and eccentricities greater than 0.8. Highlighted in blue are the regions considered to be representative of single cells. The black lines correspond to the empirical cumulative distribution functions for the parameter of interest. (B) A representative final segmentation mask in which segmented are shown in cyan over the phase contrast image.

where $\langle I_{R>0}\rangle$ is the mean fluorescence intensity of cells expressing LacI repressors, $\langle I_{\mathrm{auto}}\rangle$ is the mean intensity of cells expressing only the mCherry volume marker, and $\langle I_{R\,=\,0}\rangle$ is the mean fluorescence intensity of cells in the absence of LacI repressors. These fold-change values were very similar to those obtained through flow cytometry and were well described using the thermodynamic parameters used in the main text. With these experimentally measured fold-change values, the best-fit parameter values of the model were inferred and compared to those obtained from flow cytometry.

C.4 Parameter Estimation and Comparison

To confirm quantitative consistency between flow cytometry and microscopy, the parameter values of K_A and K_I were also estimated from three biological replicates of IPTG titration curves obtained by microscopy for strains with $R = 260$ and operators O1 and O2. Fig. S9(A) shows the data from these measurements (orange circles) and the ten biological replicates from our flow cytometry measurements (blue circles), along with the fold-change predictions from each inference. In comparison with the values obtained by flow cytometry, each parameter estimate overlapped with the 95% credible region of our flow cytometry estimates, as shown in Fig. S9(B). Specifically, these values were $K_A = 142^{+40}_{-34}\ \mu$M and $K_I = 0.6^{+0.1}_{-0.1}\ \mu$M from microscopy and $K_A = 149^{+14}_{-12}\ \mu$M and $K_I = 0.57^{+0.03}_{-0.02}\ \mu$M from the flow cytometry data. We note that the credible regions from the microscopy data shown in Fig. S9(B) are much broader than those from flow cytometry due to the fewer number of replicates performed.
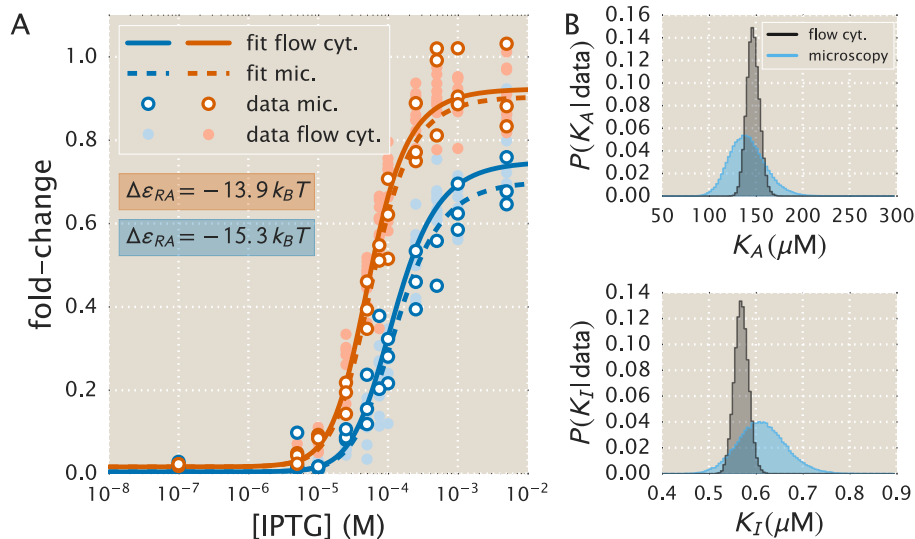
Figure S9. Comparison of measured fold-change between flow cytometry and single-cell microscopy. (A) Experimentally measured fold-change values obtained through single-cell microscopy and flow cytometry are shown as white filled and solid colored circles respectively. Solid and dashed lines indicate the predicted behavior using the most likely parameter values of K_A and K_I inferred from flow cytometry data and microscopy data, respectively. The red and blue plotting elements correspond to the different operators O1 and O2 with binding energies $\Delta\varepsilon_{RA}$ of -13.9 k_BT and -15.3 k_BT, respectively [8]. (B) The marginalized posterior distributions for K_A and K_I are shown in the top and bottom panel respectively. The posterior distribution determined using the microscopy data is wider than that computed using the flow cytometry data due to a smaller collection of data sets (three for microscopy and ten for flow cytometry).

D Inferring Allosteric Parameters from Previous Data

The fold-change profile described by Eq. (5) features three unknown parameters K_A, K_I, and $\Delta\varepsilon_{AI}$. In this section, we explore different conceptual approaches to determining these parameters. We first discuss how the induction titration profile of the simple repression constructs used in this paper are not sufficient to determine all three MWC parameters simultaneously, since multiple degenerate sets of parameters can produce the same fold-change response. We then utilize an additional data set from Brewster *et al.* [7] to determine the parameter $\Delta\varepsilon_{AI} = 4.5\ k_B T$, after which the remaining parameters K_A and K_I can be extracted from any induction profile with no further degeneracy.

D.1 Degenerate Parameter Values

In this section, we discuss how multiple sets of parameters may yield identical fold-change profiles. More precisely, we shall show that if we try to fit the data in Fig. 4C to the fold-change Eq. (5) and extract the three unknown parameters (K_A, K_I, and $\Delta\varepsilon_{AI}$), then multiple degenerate parameter sets would yield equally good fits. In other words, this data set alone is insufficient to uniquely determine the actual physical parameter values of the system. This problem persists even when fitting multiple data sets simultaneously as in Appendix E.

In Fig. S10A, we fit the $R = 260$ data by fixing $\Delta\varepsilon_{AI}$ to the value shown on the x-axis and letting the K_A and K_I parameters fit freely. We use the fold-change function Eq. (5) but with $\beta\Delta\varepsilon_{RA}$ modified to the form $\beta\Delta\tilde{\varepsilon}_{RA}$ in Eq. (S12) to account for the underlying assumptions used when fitting previous data (see Appendix D.2 for a full explanation of why this modification is needed).

The best-fit curves for several different values of $\Delta\varepsilon_{AI}$ are shown in Fig. S10B. Note that these fold-change curves are nearly overlapping, demonstrating that different sets of parameters can yield nearly equivalent responses. Without more data, the relationships between the parameter values shown in Fig. S10A represent the maximum information about the parameter values that can be extracted from the data. Additional experiments which independently measure any of these unknown parameters could resolve this degeneracy. For example, NMR measurements could be used to directly measure the fraction $(1 + e^{-\beta\Delta\varepsilon_{AI}})^{-1}$ of active repressors in the absence of IPTG [11,12].
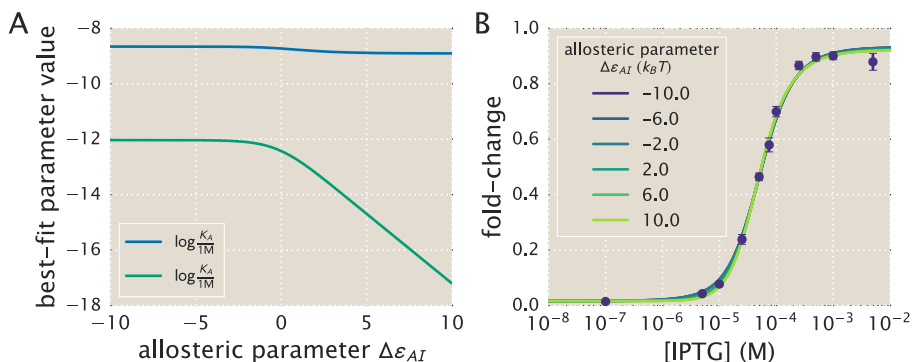
Figure S10. Multiple sets of parameters yield identical fold-change responses. (A) The data for the O2 strain ($\Delta\varepsilon_{RA} = -13.9\ k_B T$) with $R = 260$ in Fig. 4C was fit using Eq. (5) with $n = 2$. $\Delta\varepsilon_{AI}$ is forced to take on the value shown on the x-axis, while the K_A and K_I parameters are fit freely. (B) The resulting best-fit functions for several value of $\Delta\varepsilon_{AI}$ all yield nearly identical fold-change responses.

D.2 Computing $\Delta\varepsilon_{AI}$

As shown in the previous section, the fold-change response of a single strain is not sufficient to determine the three MWC parameters (K_A, K_I, and $\Delta\varepsilon_{AI}$), since degenerate sets of parameters yield nearly identical fold-change responses. To circumvent this degeneracy, we now turn to some previous data from

the *lac* system in order to determine the value $\Delta\varepsilon_{AI}$ in Eq. (5) for the induction of the Lac repressor. Specifically, we consider two previous sets of work from: (1) Garcia *et al.* [8] and (2) Brewster *et al.* [7], both of which measured fold-change with the same simple repression system in the absence of inducer ($c = 0$) but at various repressor copy numbers R. The original analysis for both data sets assumed that in the absence of inducer all of the Lac repressors were in the active state. As a result, the effective binding energies they extracted were a convolution of the DNA binding energy $\Delta\varepsilon_{RA}$ and the allosteric energy difference $\Delta\varepsilon_{AI}$ between the Lac repressor's active and inactive states. We refer to this convoluted energy value as $\Delta\tilde{\varepsilon}_{RA}$. We first deconvolute the relationship between these parameters in Garcia *et al.* and then use this relationship to extract the value of $\Delta\varepsilon_{AI}$ from the Brewster *et al.* dataset.

First, Garcia *et al.* determined the total repressor copy numbers R of different strains using quantitative Western blots. Then they measured the fold-change at these repressor copy numbers for simple repression constructs carrying the O1, O2, O3, and Oid *lac* operators integrated into the chromosome. These data were then fit to the following thermodynamic model to determine the repressor-operator DNA binding energies $\Delta\tilde{\varepsilon}_{RA}$ of each operator,

$$\text{fold-change}(c = 0) = \left(1 + \frac{R}{N_{NS}}e^{-\beta\Delta\tilde{\varepsilon}_{RA}}\right)^{-1}. \tag{S9}$$

Note that this functional form does not exactly match our fold-change Eq. (5) in the limit $c = 0$,

$$\text{fold-change}(c = 0) = \left(1 + \frac{1}{1 + e^{-\beta\Delta\varepsilon_{AI}}}\frac{R}{N_{NS}}e^{-\beta\Delta\varepsilon_{RA}}\right)^{-1}, \tag{S10}$$

since it does not account for the factor $\frac{1}{1+e^{-\beta\Delta\varepsilon_{AI}}}$ which denotes the fraction of repressors that are in the active state in the absence of inducer,

$$\frac{1}{1 + e^{-\beta\Delta\varepsilon_{AI}}} = \frac{R_A}{R}. \tag{S11}$$

In terms of our notation, the convoluted energy values $\Delta\tilde{\varepsilon}_{RA}$ extracted by Garcia *et al.* (namely, $\Delta\tilde{\varepsilon}_{RA} = -15.3\ k_BT$ for O1 and $\Delta\tilde{\varepsilon}_{RA} = -17.0\ k_BT$ for Oid) represent

$$\beta\Delta\tilde{\varepsilon}_{RA} = \beta\Delta\varepsilon_{RA} - \log\left(\frac{1}{1 + e^{-\beta\Delta\varepsilon_{AI}}}\right). \tag{S12}$$

Note that if $e^{-\beta\Delta\varepsilon_{AI}} \ll 1$, then nearly all of the repressors are active in the absence of inducer so that $\Delta\tilde{\varepsilon}_{RA} \approx \Delta\varepsilon_{RA}$.

In simple repression systems where we definitively know the value of $\Delta\varepsilon_{RA}$, it is possible to extract the value of $\Delta\varepsilon_{AI}$ by fitting theory curves to experimental simple repression data; this is because a decrease in $\Delta\varepsilon_{AI}$ in Eq. (S10) causes a distinctive rightward shift in the fold-change curve as the number of active repressors is reduced (see Fig. S11A), particularly when $\Delta\varepsilon_{AI}$ is negative. For positive values of $\Delta\varepsilon_{AI}$ the shift is much less dramatic, as demonstrated by the minimal effect on fold-change for positive $\Delta\varepsilon_{AI}$ and $c = 0$ shown in Fig. S11B. Importantly, it is impossible to determine the individual contributions of $\Delta\varepsilon_{AI}$ and $\Delta\varepsilon_{RA}$ in systems where we only know the convolved energy value $\Delta\tilde{\varepsilon}_{RA}$. In order to explicitly fix the $\Delta\varepsilon_{AI}$ parameter, we instead turn to a slightly different set of experiments.

A variation on simple repression in which multiple copies of the promoter are available for repressor binding (for instance, when the simple repression construct is on plasmid) can be used to circumvent the problems that arise when using $\Delta\tilde{\varepsilon}_{RA}$. This is because the behavior of the system is distinctly different when R_A is less than or greater than the number of promoters N. Given repression data for plasmids with known copy number N allows us to perform a fit for the value of R_A, which allows us to determine $\Delta\varepsilon_{AI}$ using Eq. (S11). To perform such an analysis, we use the measured values of $\Delta\tilde{\varepsilon}_{RA}$ and $\Delta\tilde{\varepsilon}_{RA}$ for O1 and Oid from Garcia *et al.* together with the relation Eq. (S12), and turn to data from Brewster *et al.* in order to determine the value of $\Delta\varepsilon_{AI}$. Specifically, we consider fold-change data for a system
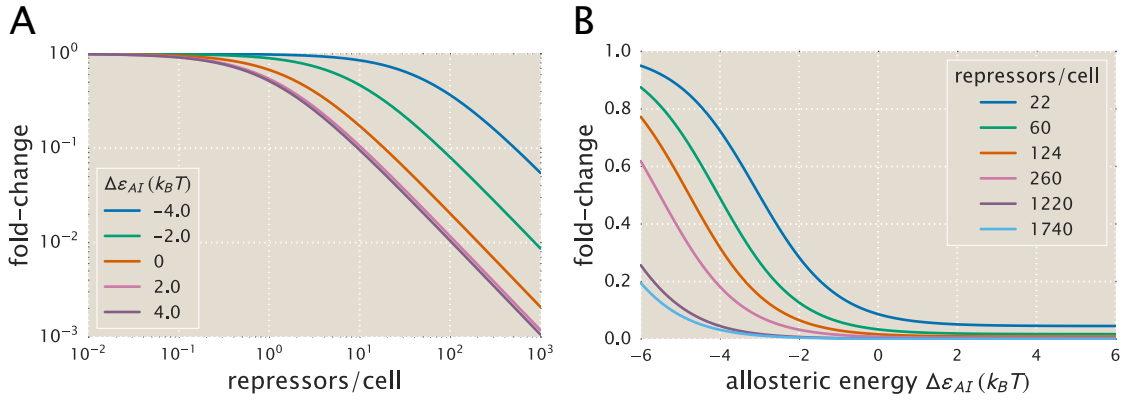
Figure S11. Effect of $\Delta\varepsilon_{AI}$ on simple repression systems. For a fixed binding energy $\Delta\varepsilon_{RA}$ of the repressor to the operator, varying the allosteric energy difference $\Delta\varepsilon_{AI}$ between the active and inactive repressor states significantly shifts the fold-change profile. (A) Simple repression titration curves (modeled here for $\Delta\varepsilon_{RA} = -15.3\ k_BT$, $c = 0$) shift dramatically to the right for negative values of $\Delta\varepsilon_{AI}$. (B) The fold-change at $c = 0$ approaches zero when $\Delta\varepsilon_{AI} > 0$, but grows large for $\Delta\varepsilon_{AI} < 0$.

with multiple identical copies of the *lac* gene expressed on plasmid with known copy numbers, using a thermodynamic model (see Eq. (4) of [7]) with the functional form

$$\text{fold-change}(c = 0) = \frac{\sum_{m=0}^{\min(N,R_A)} \frac{R_A!}{(N_{NS})^m (R_A - m)!}\binom{N}{m} e^{-m\beta\Delta\varepsilon_{RA}} (N - m)}{\sum_{m=0}^{\min(N,R_A)} \frac{R_A!}{(N_{NS})^m (R_A - m)!}\binom{N}{m} e^{-m\beta\Delta\varepsilon_{RA}}}. \tag{S13}$$

Fold-change was measured for strains with known R and $\Delta\tilde{\varepsilon}_{RA}$. Three plasmids with known copy number N were used together with $N_{NS} = 4.6 \times 10^6$ given by the length of the *E. coli* genome. Thus, after applying Eqs. (S11) and (S12), the only unknown parameter in Eq. (S13) is the $\Delta\varepsilon_{AI}$ dependence within R_A.

Fig. S12A shows how tuning $\Delta\varepsilon_{AI}$ leads to significantly different fold-change response curves. It should be noted that these different responses occur in spite of the fact that the energy term used for these curves is the convolved energy $\Delta\tilde{\varepsilon}_{AI}$. Thus, analyzing the specific fold-change response of any strain with a known plasmid copy number N will fix $\Delta\varepsilon_{AI}$. Interestingly, the inflection point of Eq. (S13) occurs near $R_A = N$, so that merely knowing where the fold-change response transitions from concave down to concave up is sufficient to determine $\Delta\varepsilon_{AI}$. In addition, once the energy gets sufficiently large ($\Delta\varepsilon_{AI} \gtrsim 5\ k_BT$), nearly all of the repressors are in the active state and increasing $\Delta\varepsilon_{AI}$ further does not affect the fold-change.

Fig. S12B shows measurements of fold-change for two O1 promoters with $N = 64$ and $N = 52$ copy numbers and one Oid promoter with $N = 10$ from Brewster *et al.* [7]. By fitting this data to Eq. (S13), we extracted the parameter value $\Delta\varepsilon_{AI} = 4.5\ k_BT$. Substituting this value into Eq. (S11) shows that 99% of the repressors are in the active state in the absence of inducer and $\Delta\tilde{\varepsilon}_{RA} \approx \Delta\varepsilon_{RA}$, so that all of the previous energies and calculations made by Garcia *et al.* and Brewster *et al.* were very accurate.
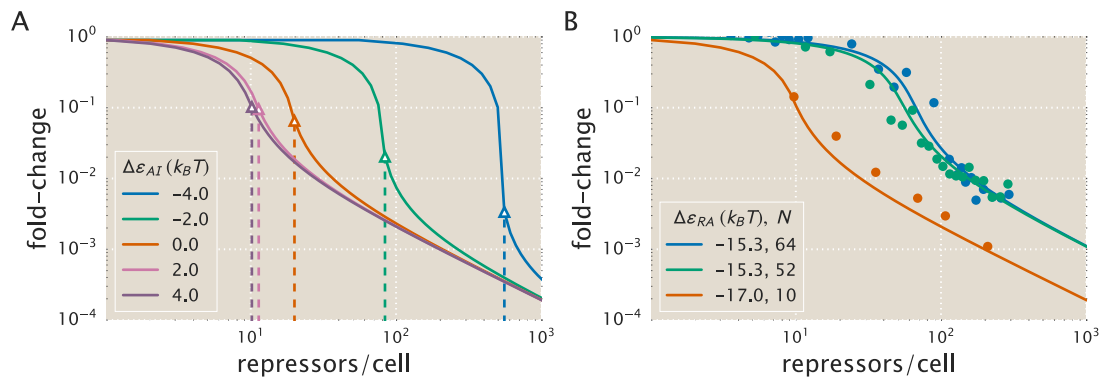
Figure S12. Fold-change of multiple identical genes. (A) In the presence of $N = 10$ identical promoters, the fold-change Eq. (S13) depends strongly on the allosteric energy difference $\Delta\varepsilon_{AI}$ between the Lac repressor's active and inactive states. The vertical dotted lines represent the number of repressors at which $R_A = N$ for each value of $\Delta\varepsilon_{AI}$. (B) Using fold-change measurements from [7] for the operators and gene copy numbers shown, we can determine the most likely value $\Delta\varepsilon_{AI} = 4.5\ k_B T$ for LacI.

E Global Fit of All Parameters

In the main text, we used the repressor copy numbers R and repressor-DNA binding energies $\Delta\varepsilon_{RA}$ as reported by Garcia and Phillips [8]. However, any error in these previous measurements of R and $\Delta\varepsilon_{RA}$ will necessarily propagate into our own fold-change predictions. In this section we take an alternative approach to fitting the physical parameters of the system to that used in the main text. First, rather than fitting only a single strain, we fit the entire data set in Fig. 5 along with microscopy data for the synthetic operator Oid (see Appendix F). In addition, we also simultaneously fit the parameters R and $\Delta\varepsilon_{RA}$ using the prior information given by the previous measurements. By using the entire data set and fitting all of the parameters, we obtain the best possible characterization of the statistical mechanical parameters of the system given our current state of knowledge.

To fit all of the parameters simultaneously we follow a similar approach to the one detailed in the Methods section. Briefly, we perform a Bayesian parameter estimation of the dissociation constants K_A and K_I, the six different repressor copy numbers R corresponding to the six *lacI* ribosomal binding sites used in our work, and the four different binding energies $\Delta\varepsilon_{RA}$ characterizing the four distinct operators used to make the experimental strains. As in the main text, we fit the logarithms $\tilde{k}_A = -\log\frac{K_A}{1\,\mathrm{M}}$ and $\tilde{k}_I = -\log\frac{K_I}{1\,\mathrm{M}}$ of the dissociation constants which grants better numerical stability.

We begin by writing Bayes' theorem,

$$P(\tilde{k}_A, \tilde{k}_I, \boldsymbol{R}, \boldsymbol{\Delta\varepsilon_{RA}} \mid D) = \frac{P(D \mid \tilde{k}_A, \tilde{k}_I, \boldsymbol{R}, \boldsymbol{\Delta\varepsilon_{RA}})P(\tilde{k}_A, \tilde{k}_I, \boldsymbol{R}, \boldsymbol{\Delta\varepsilon_{RA}})}{P(D)}, \tag{S14}$$

where $\boldsymbol{R}$ is an array containing the six different repressor copy numbers to be fit, $\boldsymbol{\Delta\varepsilon_{RA}}$ is an array containing the four binding energies to be fit, and D is the experimental fold-change data. The term $P(\tilde{k}_A, \tilde{k}_I, \boldsymbol{R}, \boldsymbol{\Delta\varepsilon_{RA}} \mid D)$ gives the probability distributions of all of the parameters given the data. The term $P(D \mid \tilde{k}_A, \tilde{k}_I, \boldsymbol{R}, \boldsymbol{\Delta\varepsilon_{RA}})$ represents the likelihood of having observed our experimental data given some value for each parameter. $P(\tilde{k}_A, \tilde{k}_I, \boldsymbol{R}, \boldsymbol{\Delta\varepsilon_{RA}})$ contains all the prior information on the values of these parameters. Lastly, $P(D)$ serves as a normalization constant and hence can be ignored.

As in Eqs. (12) and (13), we assume that deviations of the experimental fold-change from the theoretical predictions are normally distributed with mean zero and standard deviation σ. Given n independent measurements of the fold-change, the first term in Eq. (S14) can be written as

$$P(\tilde{k}_A, \tilde{k}_I, \boldsymbol{R}, \boldsymbol{\Delta\varepsilon_{RA}}, \sigma \mid D) = \frac{1}{(2\pi\sigma^2)^{\frac{n}{2}}} \prod_{i=1}^{n} \exp\left[-\frac{(\mathrm{fc}_{\exp}^{(i)} - \mathrm{fc}(\tilde{k}_A, \tilde{k}_I, R^{(i)}, \Delta\varepsilon_{RA}^{(i)}, c^{(i)}))^2}{2\sigma^2} \right], \tag{S15}$$

where $\mathrm{fc}_{\exp}^{(i)}$ is the ith experimental fold-change and $\mathrm{fc}(\cdots)$ is the theoretical prediction. Note that the standard deviation σ of this distribution is not known and hence needs to be included as a parameter to be fit.

The second term in Eq. (S14) represents the prior information of the parameter values. We assume that all parameters are independent of each other, so that

$$P(\tilde{k}_A, \tilde{k}_I, \boldsymbol{R}, \boldsymbol{\Delta\varepsilon_{RA}}, \sigma) = P(\tilde{k}_A) \cdot P(\tilde{k}_I) \cdot \prod_i P(R^{(i)}) \cdot \prod_j P(\Delta\varepsilon_{RA}^{(j)}) \cdot P(\sigma), \tag{S16}$$

where the superscript (i) indicates the repressor copy number of index i and the superscript (j) denotes the binding energy of index j. As above, we note that a prior must also be included for the unknown parameter σ.

Because we knew nothing about the values of $\tilde{k}_A$, $\tilde{k}_I$, and σ before performing the experiment, we assign maximally uninformative priors to each of these parameters. More specifically, we assign uniform priors to $\tilde{k}_A$ and $\tilde{k}_I$ and a Jeffreys prior to σ [13]. We do, however, have prior information for the repressor copy numbers and the repressor-DNA binding energies from Ref. [8]. This prior knowledge is included within our model using an informative prior for these two parameters, which we assume to be

Gaussian for simplicity. Hence each of the $R^{(i)}$ repressor copy numbers to be fit satisfies

$$P(R^{(i)}) = \frac{1}{\sqrt{2\pi\sigma_{R_i}^2}} \exp\left(-\frac{(R^{(i)} - \bar{R}^{(i)})^2}{2\sigma_{R_i}^2}\right),$$ (S17)

where $\bar{R}^{(i)}$ is the mean repressor copy number as reported in [8], and σ_{R_i} is the variability associated with this parameter. Since this is an informative prior, we use the given value of σ_{R_i} from previous measurements rather than leaving it as a free parameter.

The binding energies $\Delta\varepsilon_{RA}^{(j)}$ are also assumed to have a Gaussian informative prior of the same form. We write it as

$$P(\Delta\varepsilon_{RA}^{(j)}) = \frac{1}{\sqrt{2\pi\sigma_{\varepsilon_j}^2}} \exp\left(-\frac{(\Delta\varepsilon_{RA}^{(j)} - \Delta\bar{\varepsilon}_{RA}^{(j)})^2}{2\sigma_{\varepsilon_j}^2}\right),$$ (S18)

where $\Delta\bar{\varepsilon}_{RA}^{(j)}$ is the binding energy as inferred in [8] and σ_{ε_j} is the variability associated with the parameter around the mean value reported.

The σ_{R_i} and σ_{ε_j} parameters will constrain the range of values for $R^{(i)}$ and $\Delta\varepsilon_{RA}^{(j)}$ found from the fitting. For example, if for some i the standard deviation σ_{R_i} is very small, it implies a strong confidence in the previously reported value. Mathematically, the exponential in Eq. (S17) will ensure that the best-fit $R^{(i)}$ lies within a few standard deviations of $\bar{R}^{(i)}$. Since we are interested in exploring which values could give the best fit, the errors are taken to be wide enough to allow the parameter estimation to freely explore parameter space in the vicinity of the best estimates. Putting all these terms together, we use Markov chain Monte Carlo to sample the posterior distribution $P(\tilde{k}_A, \tilde{k}_I, \boldsymbol{R}, \boldsymbol{\Delta\varepsilon_{RA}}, \sigma \mid D)$. This allows us to determine both the most likely value for each physical parameter as well as its associated credible regions (see GitHub repository for the implementation).

Fig. S13 shows the result of this global fit. When compared with Fig. 5 we can see that fitting for the binding energies and the repressor copy numbers improves the agreement between the theory and the data. Table S2 summarizes the values of the parameters as obtained with this MCMC parameter inference. We note that even though we allowed the repressor copy numbers and repressor-DNA binding energies to vary, the resulting fit values were very close to the previously reported values. The fit values of the repressor copy numbers were all within one standard deviation of the previous reported values provided in Ref. [8]. And although some of the repressor-DNA binding energies differed by a few standard deviations from the reported values, the differences were always less than 1 $k_B T$, which represents a small change in the biological scales we are considering. The biggest discrepancy between our fit values and the previous measurements arose for the synthetic Oid operator, which we discuss in more detail in Appendix F.
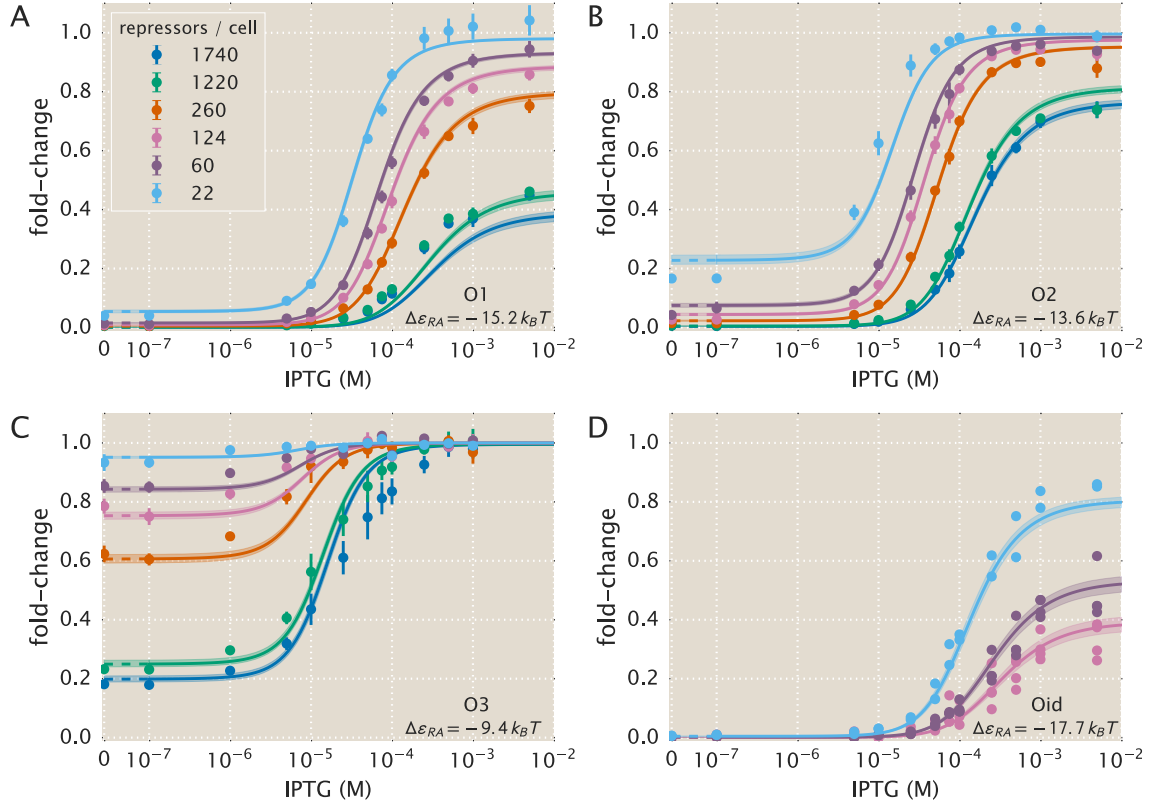
Figure S13. Global fit of dissociation constants, repressor copy numbers and binding energies. Theoretical predictions resulting from simultaneously fitting the dissociation constants K_A and K_I, the six repressor copy numbers R, and the four repressor-DNA binding energies $\Delta\varepsilon_{RA}$ using the entire data set from Fig. 5 as well as the microscopy data for the Oid operator. Error bars of experimental data show the standard error of the mean (eight or more replicates) and shaded regions denote the 95% credible region. For the Oid operator, all of the data points are shown since a smaller number of replicates were taken. The shaded regions are significantly smaller than in Fig. 5 because this fit was based on all data points, and hence the fit parameters are much more tightly constrained. The dashed lines at 0 IPTG indicates a linear scale, whereas solid lines represent a log scale.

Table S2. Global fit of all parameter values using the entire data set in Fig. 5. In addition to fitting the repressor inducer dissociation constants K_A and K_I as was done in the text, we also fit the repressor DNA binding energy $\Delta\varepsilon_{RA}$ as well as the repressor copy numbers R for each strain. The middle columns show the previously reported values for all $\Delta\varepsilon_{RA}$ and R values, with $\pm$ representing the standard deviation of three replicates. The right column shows the global fits from this work, with the subscript and superscript notation denoting the 95% credible region. Note that there is overlap between all of the repressor copy numbers and that the net difference in the repressor-DNA binding energies is less than 1 k_BT.

	Reported Values [8]	Global Fit
$\tilde{k}_A$	$-$	$-5.33^{+0.06}_{-0.05}$
$\tilde{k}_I$	$-$	$0.31^{+0.05}_{-0.06}$
K_A	$-$	$205^{+11}_{-12}\,\mu\mathrm{M}$
K_I	$-$	$0.73^{+0.04}_{-0.04}\,\mu\mathrm{M}$
R_{22}	22 ± 4	20^{+1}_{-1}
R_{60}	60 ± 20	74^{+4}_{-3}
R_{124}	124 ± 30	130^{+6}_{-6}
R_{260}	260 ± 40	257^{+9}_{-11}
R_{1220}	1220 ± 160	1191^{+32}_{-55}
R_{1740}	1740 ± 340	1599^{+75}_{-87}
O1 $\Delta\varepsilon_{RA}$	$-15.3 \pm 0.2\ k_BT$	$-15.2^{+0.1}_{-0.1}\ k_BT$
O2 $\Delta\varepsilon_{RA}$	$-13.9 \pm 0.2\ k_BT$	$-13.6^{+0.1}_{-0.1}\ k_BT$
O3 $\Delta\varepsilon_{RA}$	$-9.7 \pm 0.1\ k_BT$	$-9.4^{+0.1}_{-0.1}\ k_BT$
Oid $\Delta\varepsilon_{RA}$	$-17.0 \pm 0.2\ k_BT$	$-17.7^{+0.2}_{-0.1}\ k_BT$

# F   Applicability of Theory to the Oid Operator Sequence

In addition to the native operator sequences (O1, O2, and O3) considered in the main text, we were also interested in testing our model predictions against the synthetic Oid operator. In contrast to the other operators, Oid is one base pair shorter in length (20 bp) and is known to provide stronger repression than the native operator sequences considered so far. While the theory should be similarly applicable, measuring the lower fold-changes associated with this YFP construct was expected to be near the sensitivity limit for our flow cytometer, due to the especially strong binding energy of Oid ($\Delta\varepsilon_{RA} = -17.0\ k_BT$) [6]. Accordingly, fluorescence data for Oid were obtained using microscopy rather than flow cytometery.

To test the predictions, we follow the approach of the main text and make fold-change predictions based on the parameter estimates from our strain with $R = 260$ and an O2 operator. These predictions are shown in Fig. S14A, where we also plot data taken in triplicate for strains containing $R = 22$, 60, and 124, obtained by single-cell microscopy. We find that the data is systematically below the theoretical predictions. We also considered our global fitting approach to see whether we might find better agreement with the observed data. Interestingly, we find that the parameters remain largely unchanged, except that our estimate for the Oid binding energy $\Delta\varepsilon_{RA}$ is shifted to $-17.7\ k_BT$ instead of the value $-17.0\ k_BT$ found by Garcia *et al.* [8]. In Fig. S14B we again plot the Oid fold-change data but with theoretical predictions using the new estimate for the Oid binding energy from our global fit (see Appendix E).
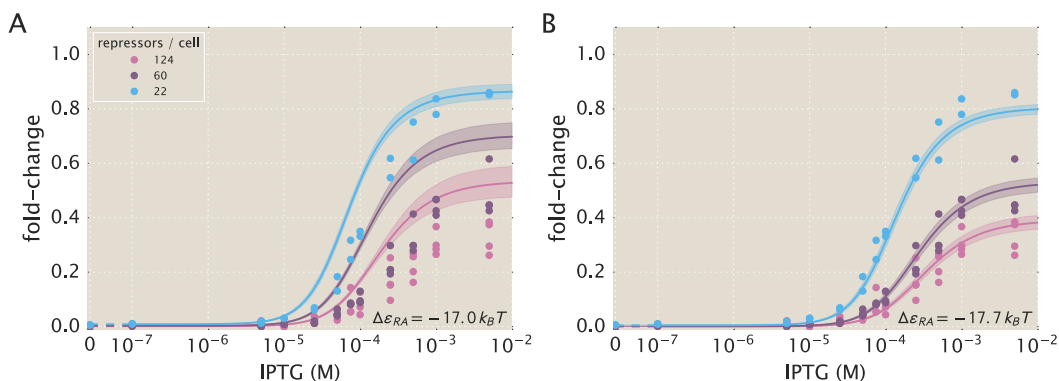
Figure S14. Predictions of fold-change for strains with an Oid binding sequence versus experimental measurements with different repressor copy numbers. (A) Experimental data is plotted against the parameter-free predictions that are based on our fit to the O2 strain with $R = 260$. Here we use the previously measured binding energy $\Delta\varepsilon_{RA} = -17.0\ k_BT$ [8]. (B) The same experimental data is plotted against the best-fit parameters using the entire data set O1, O2, O3, and Oid data sets to infer K_A, K_I, repressor copy numbers, and the binding energies of all operators (see Appendix E). Here the major difference in the inferred parameters is a shift in the binding energy for Oid from $\Delta\varepsilon_{RA} = -17.0\ k_BT$ to $\Delta\varepsilon_{RA} = -17.7\ k_BT$, which now shows agreement between the theoretical predictions and experimental data. Shaded regions from the theoretical curves denote the 95% credible region. These are narrower in Part B because the inference of parameters was performed with much more data, and hence the best-fit values are more tightly constrained. Individual data points are shown due to the small number of replicates. The dashed lines at 0 IPTG indicates a linear scale, whereas solid lines represent a log scale.

Fig. S15 shows the cumulative data from Garcia *et al.* [8], Brewster *et al.* [7], as well as our data with $c = 0\ \mu M$, which all measured fold-change for the same simple repression architecture utilizing different reporters and measurement techniques. We find that a binding energy for Oid $\Delta\varepsilon_{RA} = -17.7\ k_BT$ still compares reasonably well with all previous measurements.
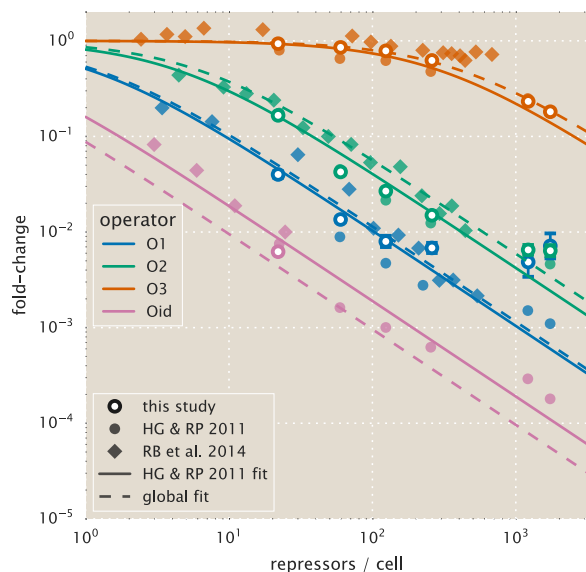
Figure S15. Comparison of fold-change predictions based on binding energies from Garcia *et al.* and those inferred from this work. Fold-change curves for the different repressor-DNA binding energies $\Delta\varepsilon_{RA}$ are plotted as a function of repressor copy number when IPTG concentration $c = 0$. Solid curves use the binding energies determined from Garcia *et al.* [8], while the dashed curves use the inferred binding energies we obtained when performing a global fit of K_A, K_I, repressor copy numbers, and the binding energies using all available data from our work. Fold-change measurements from our experiments (outlined circles) [8] (solid circles), and [7] (diamonds) show that the small shifts in binding energy that we infer are still in agreement with prior data. Note that only a single data flow cytometry data point is shown for Oid from this study, since the $R = 60$ and $R = 124$ curves from Fig. S14 had extremely low fold-change in the absence of inducer ($c = 0$) as to be indistinguishable from autofluorescence, and in fact their fold-change values in this limit were negative and hence do not appear on this plot.

G Properties of Induction Titration Curves

In this section, we discuss five physiologically important properties of an induction profile which are shown schematically in Fig. S16: the leakiness, saturation, dynamic range, $[EC_{50}]$, and effective Hill coefficient. These results build upon extensive work by Martins and Swain, who computed many such properties for ligand-receptor binding within the MWC model [14]. Here we extend their work into the realm of induction.
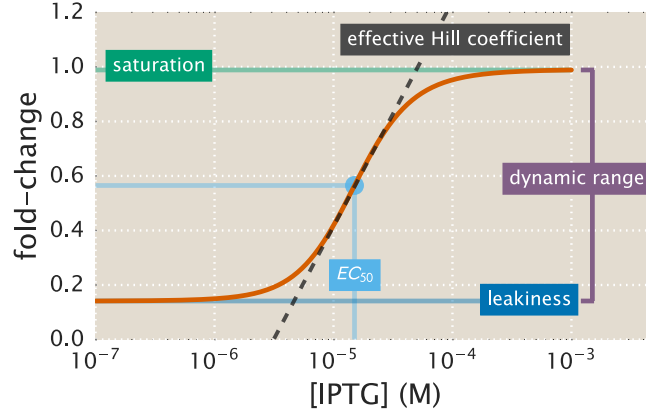
Figure S16. The leakiness, dynamic range, $[EC_{50}]$, and effective Hill coefficient for an input-output response. The titration curve of operator O3 ($\Delta\varepsilon_{RA} = -9.7\ k_B T$) with $R = 1740$.

The leakiness is given by the minimal system response, which for simple repression is the fold-change in the absence of inducer, given by Eq. (6) as

$$\text{leakiness} = \left(1 + \frac{1}{1 + e^{-\beta\Delta\varepsilon_{AI}}} \frac{R}{N_{NS}} e^{-\beta\Delta\varepsilon_{RA}}\right)^{-1}. \tag{S19}$$

The dynamic range is the difference between the maximum system response - which for simple repression occurs at saturating ligand concentrations given by Eq. (7) - and the minimum system response,

$$\text{dynamic range} = \left(1 + \frac{1}{1 + e^{-\beta\Delta\varepsilon_{AI}}\left(\frac{K_A}{K_I}\right)^n} \frac{R}{N_{NS}} e^{-\beta\Delta\varepsilon_{RA}}\right)^{-1} - \left(1 + \frac{1}{1 + e^{-\beta\Delta\varepsilon_{AI}}} \frac{R}{N_{NS}} e^{-\beta\Delta\varepsilon_{RA}}\right)^{-1}. \tag{S20}$$

Systems that minimize leakiness repress strongly in the absence of a signal (i.e. a ligand), and systems that maximize saturation have high expression levels in the presence of a signal. Together, these two properties determine the dynamic range of a system's response. Fig. S17 shows how these properties are affected by operator binding energy and repressor copy number. These plots show that repressor copy number does not determine the system's minimum leakiness or maximum saturation and dynamic range, but it does determine the operator binding energy at which these maximum and minimum values occur.

The two remaining properties, the $[EC_{50}]$ and effective Hill coefficient, determine the horizontal properties of a system - that is, they determine the range of inducer concentration in which the system's output goes from its minimum to maximum values. The $[EC_{50}]$ denotes the inducer concentration required to generate a system response Eq. (5) halfway between its minimum and maximum value,

$$\text{fold-change}(c = [EC_{50}]) = \frac{\text{fold-change}(c = 0) + \text{fold-change}(c \to \infty)}{2}. \tag{S21}$$

S24
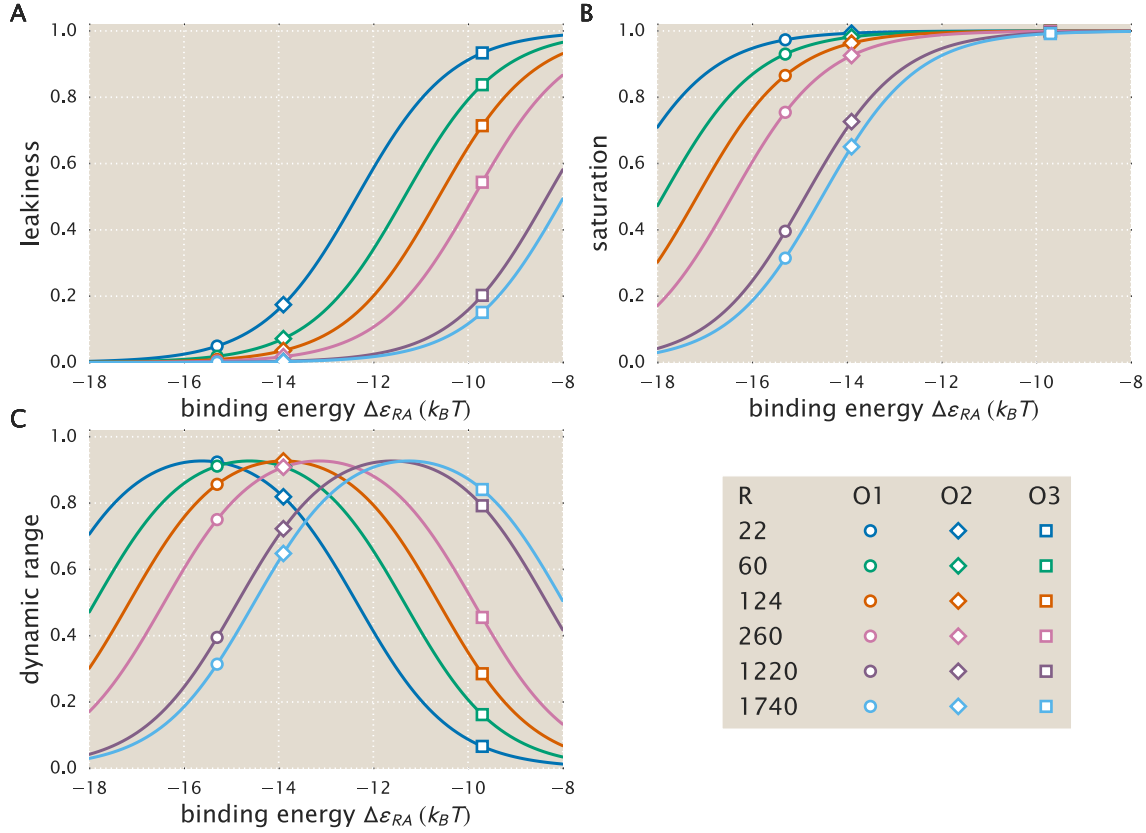
Figure S17. Leakiness and dynamic range depend on both operator binding energy and repressor copy number. (A) Leakiness values range between 0 and 1, and experience a right-shift relative to operator binding energy as repressor copy number is increased. (B) As with leakiness, curves for saturation shift right relative to operator binding energy as repressor copy number is increased. (C) Dynamic range values also shift right as repressor copy numbers increase. For small operator repressor binding energies, the leakiness is small but the saturation increases with $\Delta\varepsilon_{RA}$; for large operator repressor binding energies the saturation is near unity and the leakiness increases with $\Delta\varepsilon_{RA}$, thereby decreasing the dynamic range and causing the peaked character of the dynamic range curve. Repressor copy number does not affect the maximum dynamic range. Circles, diamonds, and squares represent $\Delta\varepsilon_{RA}$ values for the O1, O2, and O3 operators, respectively.

931 For the simple repression system, the $[EC_{50}]$ is given by

$$\frac{[EC_{50}]}{K_A} = \frac{\frac{K_A}{K_I} - 1}{\frac{K_A}{K_I} - \left(\frac{\left(1+\frac{R}{N_{NS}}e^{-\beta\Delta\varepsilon_{RA}}\right)+\left(\frac{K_A}{K_I}\right)^n\left(2e^{-\beta\Delta\varepsilon_{AI}}+\left(1+\frac{R}{N_{NS}}e^{-\beta\Delta\varepsilon_{RA}}\right)\right)}{2\left(1+\frac{R}{N_{NS}}e^{-\beta\Delta\varepsilon_{RA}}\right)+e^{-\beta\Delta\varepsilon_{AI}}+\left(\frac{K_A}{K_I}\right)^n e^{-\beta\Delta\varepsilon_{AI}}}\right)^{\frac{1}{n}}} - 1. \tag{S22}$$

932 Next, we compute the effective Hill coefficient h, which equals twice the log-log slope of the normalized
933 current evaluated at $c = [EC_{50}]$,

$$h \equiv \left(2\frac{d}{d\log c}\left[\log\left(\frac{\text{fold-change}(c) - \text{leakiness}}{\text{dynamic range}}\right)\right]\right)_{c=[EC_{50}]}. \tag{S23}$$

934 Fig. S18 shows how the $[EC_{50}]$ and effective Hill coefficient depend on operator binding energy and
935 repressor copy number. This dependence is reflected in the right-shifts and slope variations seen in
936 fold-change induction curves as repressor copy number increases. Both $[EC_{50}]$ and h vary significantly

937 with repressor copy number for sufficiently strong operator binding energies. Interestingly, for low
938 operator binding energies on the order of O3, it is predicted that the effective Hill coefficient should not
939 vary with repressor copy number.
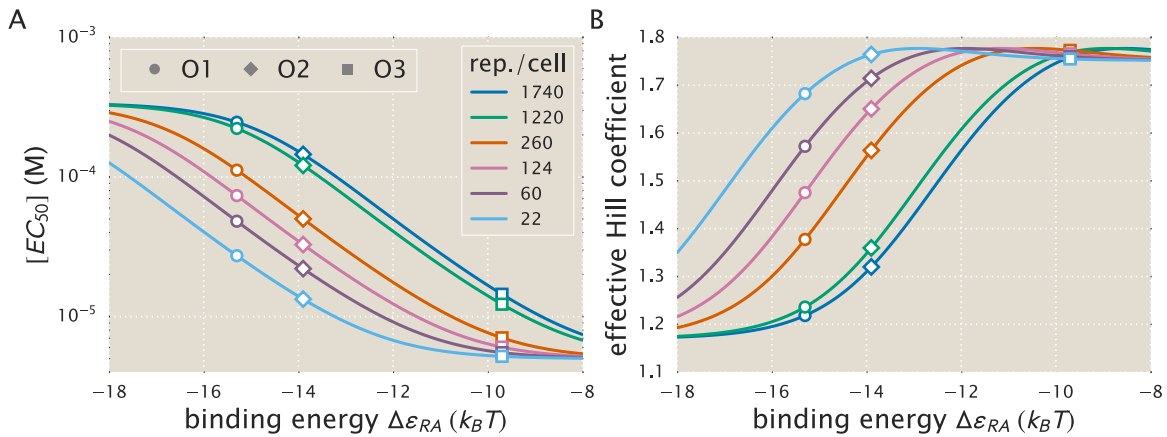
Figure S18. [EC_{50}] and effective Hill coefficient depend strongly on repressor copy number and operator binding energy. (A) [EC_{50}] values range from very small and tightly clustered at weak operator binding energies (e.g. O3) to relatively large and spread out for stronger operator binding energies (O1 and O2). (B) The effective Hill coefficient is maximized at approximately 1.75 for weak binding energies (O3), and decreases for stronger binding energies (O1 and O2). Circles, diamonds, and squares represent $\Delta\varepsilon_{RA}$ values for the O1, O2, and O3 operators, respectively.

H   Fold-Change Sensitivity Analysis

In Fig. 5 we found that the width of the credible regions varied widely depending on the repressor copy number R and repressor operator binding energy $\Delta\varepsilon_{RA}$. More precisely, the credible regions were much narrower for low repressor copy numbers R and weak binding energy $\Delta\varepsilon_{RA}$. In this section, we explain how this behavior comes about.

We focus our attention on the fold-change in the $c \to \infty$ limit given by Eq. (7), where all of the credible regions in Fig. 5 are widest. The width of the credible regions corresponds to how sensitive the fold-change is to the fit values of the dissociation constants K_A and K_I. To be quantitative, we define

$$\Delta\,\text{fold-change}_{K_A} \equiv \text{fold-change}(K_A, K_I^{\text{fit}}) - \text{fold-change}(K_A^{\text{fit}}, K_I^{\text{fit}}), \tag{S24}$$

the difference between the fold-change at a particular K_A value relative to the best-fit dissociation constant $K_A^{\text{fit}} = 139 \times 10^{-6}\,\text{M}$. For simplicity, we keep the inactive state dissociation constant fixed at its best-fit value $K_I^{\text{fit}} = 0.53 \times 10^{-6}\,\text{M}$. A larger difference $\Delta\,\text{fold-change}_{K_A}$ implies a wider credible region. Similarly, we define the analogous quantity

$$\Delta\,\text{fold-change}_{K_I} = \text{fold-change}(K_A^{\text{fit}}, K_I) - \text{fold-change}(K_A^{\text{fit}}, K_I^{\text{fit}}) \tag{S25}$$

to measure the sensitivity of the fold-change to K_I at a fixed K_A^{fit}. Fig. S19 shows both of these quantities in the limit $c \to \infty$ for different repressor-DNA binding energies $\Delta\varepsilon_{RA}$ and repressor copy numbers R. See our GitHub repository for the code that reproduces these plots.

To understand how the width of the credible region scales with $\Delta\varepsilon_{RA}$ and R, we can Taylor expand the difference in fold-change to first order, $\Delta\,\text{fold-change}_{K_A} \approx \frac{\partial\,\text{fold-change}}{\partial K_A}\left(K_A - K_A^{\text{fit}}\right)$, where the partial derivative has the form

$$\frac{\partial\,\text{fold-change}}{\partial K_A} = \frac{e^{-\beta\Delta\varepsilon_{AI}}\frac{n}{K_I}\left(\frac{K_A}{K_I}\right)^{n-1}}{\left(1 + e^{-\beta\Delta\varepsilon_{AI}}\left(\frac{K_A}{K_I}\right)^{n}\right)^{2}}\frac{R}{N_{NS}}e^{-\beta\Delta\varepsilon_{RA}}\left(1 + \frac{1}{1 + e^{-\beta\Delta\varepsilon_{AI}}\left(\frac{K_A}{K_I}\right)^{n}}\frac{R}{N_{NS}}e^{-\beta\Delta\varepsilon_{RA}}\right)^{-2}. \tag{S26}$$

Similarly, the Taylor expansion $\Delta\,\text{fold-change}_{K_I} \approx \frac{\partial\,\text{fold-change}}{\partial K_I}\left(K_I - K_I^{\text{fit}}\right)$ features the partial derivative

$$\frac{\partial\,\text{fold-change}}{\partial K_I} = -\frac{e^{-\beta\Delta\varepsilon_{AI}}\frac{n}{K_I}\left(\frac{K_A}{K_I}\right)^{n}}{\left(1 + e^{-\beta\Delta\varepsilon_{AI}}\left(\frac{K_A}{K_I}\right)^{n}\right)^{2}}\frac{R}{N_{NS}}e^{-\beta\Delta\varepsilon_{RA}}\left(1 + \frac{1}{1 + e^{-\beta\Delta\varepsilon_{AI}}\left(\frac{K_A}{K_I}\right)^{n}}\frac{R}{N_{NS}}e^{-\beta\Delta\varepsilon_{RA}}\right)^{-2}. \tag{S27}$$

From Eqs. (S26) and (S27), we find that both $\Delta\,\text{fold-change}_{K_A}$ and $\Delta\,\text{fold-change}_{K_I}$ increase in magnitude with R and decrease in magnitude with $\Delta\varepsilon_{RA}$. Accordingly, we expect that the O3 strains (with the least negative $\Delta\varepsilon_{RA}$) and the strains with the smallest repressor copy number will lead to partial derivatives with smaller magnitude and hence to tighter credible regions. Indeed, this prediction is carried out in Fig. S19.

Lastly, we note that Eqs. (S26) and (S27) enable us to quantify the scaling relationship between the width of the credible region and the two quantities R and $\Delta\varepsilon_{RA}$. For example, for the O3 strains, where the fold-change at saturating inducer concentration is ≈ 1, the right-most term in both equations which equals the fold-change squared is roughly 1. Therefore, we find that both $\frac{\partial\,\text{fold-change}}{\partial K_A}$ and $\frac{\partial\,\text{fold-change}}{\partial K_I}$ scale linearly with R and $e^{-\beta\Delta\varepsilon_{RA}}$. Thus the width of the $R = 22$ strain will be roughly 1/1000 as large as that of the $R = 1740$ strain; similarly, the width of the O3 curves will be roughly 1/1000 the width of the O1 curves.
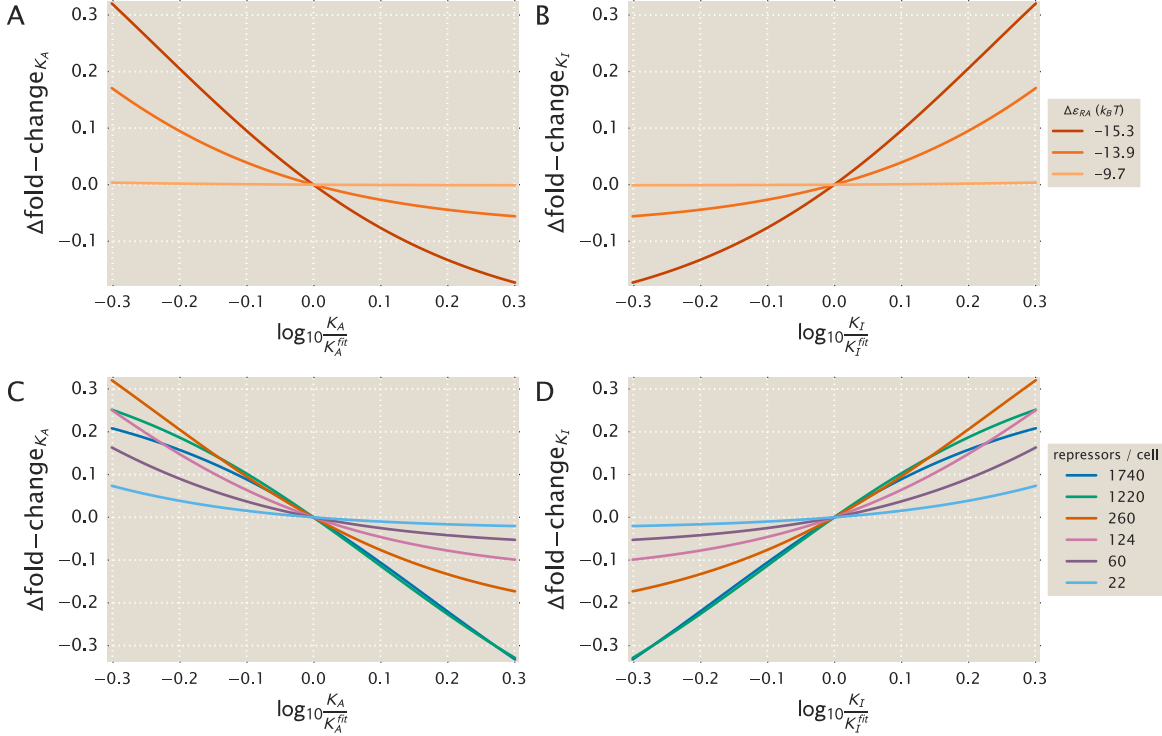
Figure S19. Determining how sensitive the fold-change values are to the fit values of the dissociation constants. (A) The difference Δ fold-change$_{K_A}$ in fold change when the dissociation constant K_A is slightly offset from its best-fit value $K_A = 139^{+29}_{-22} \times 10^{-6}$ M, as given by Eq. (S24). Fold-change is computed in the limit of saturating inducer concentration ($c \to \infty$, see Eq. (7)) where the credible regions in Fig. 5 are widest. The O3 strain ($\Delta\varepsilon_{RA} = -9.7\ k_B T$) is about 1/1000 as sensitive as the O1 operator to perturbations in the parameter values, and hence its credible region is roughly 1/1000 as wide. All curves were made using $R = 260$. (B) As in Part A, but plotting the sensitivity of fold-change to the K_I parameter relative to the best-fit value $K_I = 0.53^{+0.04}_{-0.04} \times 10^{-6}$ M. Note that only the magnitude, and not the sign, of this difference describes the sensitivity of each parameter. Hence, the O3 strain is again less sensitive than the O1 and O2 strains. (C) As in A, but showing how the fold-change sensitivity for different repressor copy numbers. The strains with lower repressor copy number are less sensitive to changes in the dissociation constants, and hence their corresponding curves in Fig. 5 have tighter credible regions. All curves were made using $\Delta\varepsilon_{RA} = -13.9\ k_B T$. (D) As in Part C, the sensitivity of fold-change with respect to K_I is again smallest (in magnitude) for the low repressor copy number strains.

I Comparison of Parameter Estimation and Fold-Change Predictions across Strains

The inferred parameter values for K_A and K_I in the main text were determined with induction fold-change measurements from a single strain ($R = 260$, $\Delta\varepsilon_{RA} = -13.9\ k_BT$, $n = 2$, and $\Delta\varepsilon_{AI} = 4.5\ k_BT$). After determining these parameters, we were able to predict the fold-change of the remaining strains without any additional fitting. Ultimately, the theory should be independent of the specific strain used to estimate K_A and K_I; using any alternative strain to fit K_A and K_I should yield similar predictions. For the sake of completeness, we demonstrate below what the corresponding predictions would be if we had used one of the other strains to fix the K_A and K_I parameters. Overall, we find that regardless of which strain is chosen to determine the unknown parameters, the predictions laid out by the theory closely match the experimental measurements.

We first take a look at how the inferred parameters K_A and K_I compare had we used a different strain to infer their values. In Fig. S20 we plot the corresponding values of these two parameters along with the global estimates using all available data. In general we find good agreement regardless of which strain is chosen, especially for strains containing an O1 or O2 operator binding site. We do note some deviation in these predictions with strains containing an O3 operator, as reflected by the larger error bars which represent the 95% highest probability credible region in the parameter inference. This is likely related to the fact that in Fig. 5, the predictions for the O3 operator were also slightly less accurate than for the O1 and O2 operators.
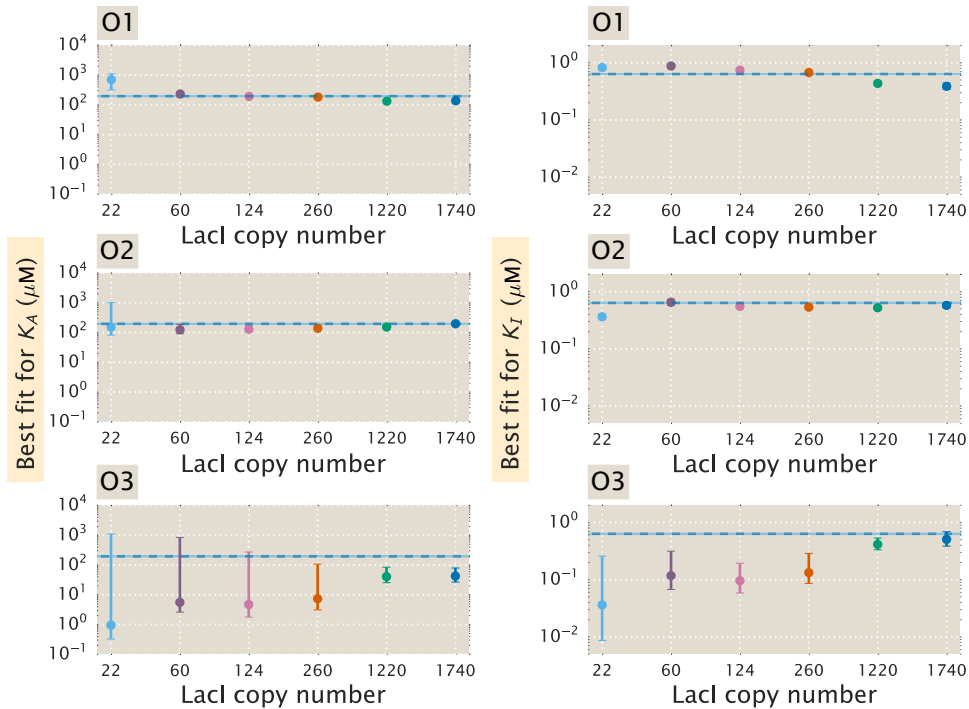

Figure S20. Inference of K_A and K_I from each strain-specific fold-change data set. K_A and K_I were separately fit to each strain's induction fold-change data set. Best fit values are grouped by operator binding site (O1, O2, and O3), with the strain's LacI copy number noted in the x-axis. Error bars denote the 95% credible region from the parameter inference. The blue dashed line shows the best estimate of K_A and K_I from our global inference with all available data across all strains.

Next we follow the approach taken in the main text and use Eq. (5) to predict fold-change for different LacI copy numbers. Here we expect the agreement between our theoretical predictions and data to hold, irrespective of the strain associated with our inference. In Fig. S21 we plot the fold-change predictions

along with experimental data for each of our strains that contains an O1 operator. To make sense of this plot consider the first row as an example. In the first row, K_A and K_I were estimated using data from the strain containing $R = 1740$ and an O1 operator (top left most plot, shaded in gray). The remaining plots in this row show the predicted fold-change using these values for K_A and K_I. Moving down a column, we then infer K_A and K_I using data from a strain containing a different repressor copy number. In Fig. S22 and Fig. S23, we similarly apply this inference to our strains with O2 and O3 operators, respectively. We note that the overwhelming majority of predictions closely match the experimental data.The notable exception is that using the $R = 22$ strain provides poor predictions for the strains with large copy numbers (especially $R = 1220$ and $R = 1740$). This loss in predictive power is due to the poorer estimates of K_A and K_I for the $R = 22$ strain shown in Eq. (S20).
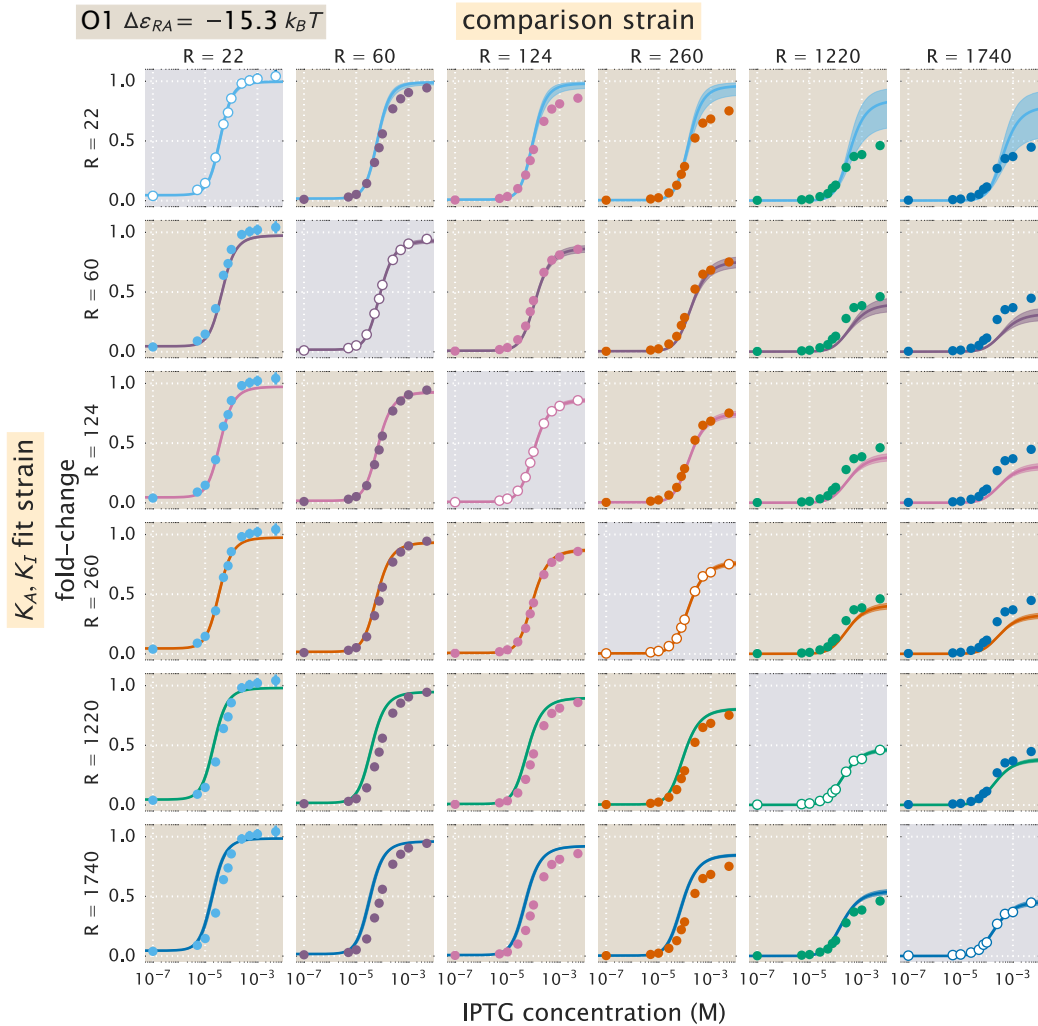
Figure S21. O1 strain fold-change predictions based on strain-specific parameter estimation of K_A and K_I. Fold-change in expression is plotted as a function of IPTG concentration for all strains containing an O1 operator. The solid points correspond to the mean experimental value. The solid lines correspond to Eq. (5) using the parameter estimates of K_A and K_I. Each row uses a single set of parameter values based on the strain noted on the left axis. The shaded plots along the diagonal are those where the parameter estimates are plotted along with the data used to infer them. Values for repressor copy number and operator binding energy are from [8]. The shaded region on the curve represents the uncertainty from our parameter estimates and reflect the 95% highest probability density region of the parameter predictions.
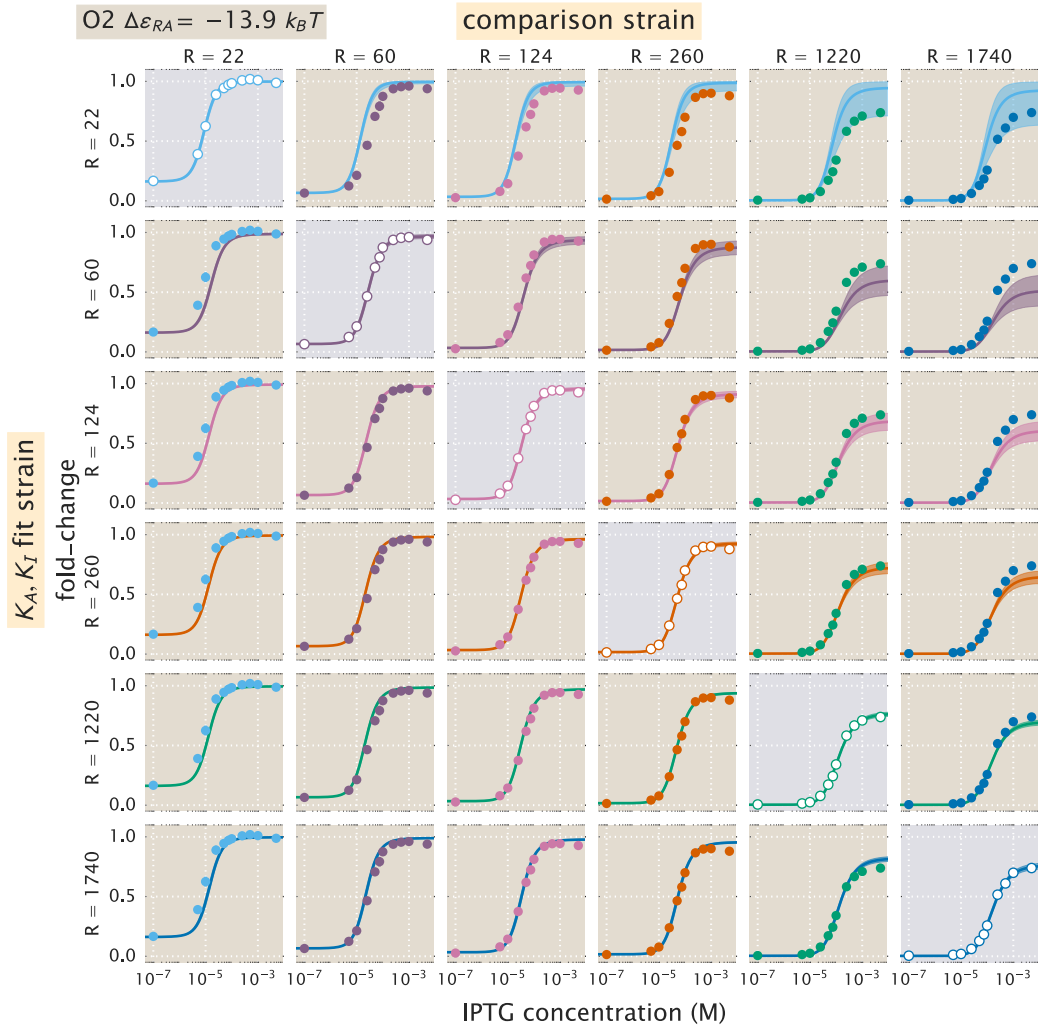
Figure S22. O2 strain fold-change predictions based on strain-specific parameter estimation of K_A and K_I. Fold-change in expression is plotted as a function of IPTG concentration for all strains containing an O2 operator. The plots and data shown are analogous to Fig. S21, but for the O2 operator.
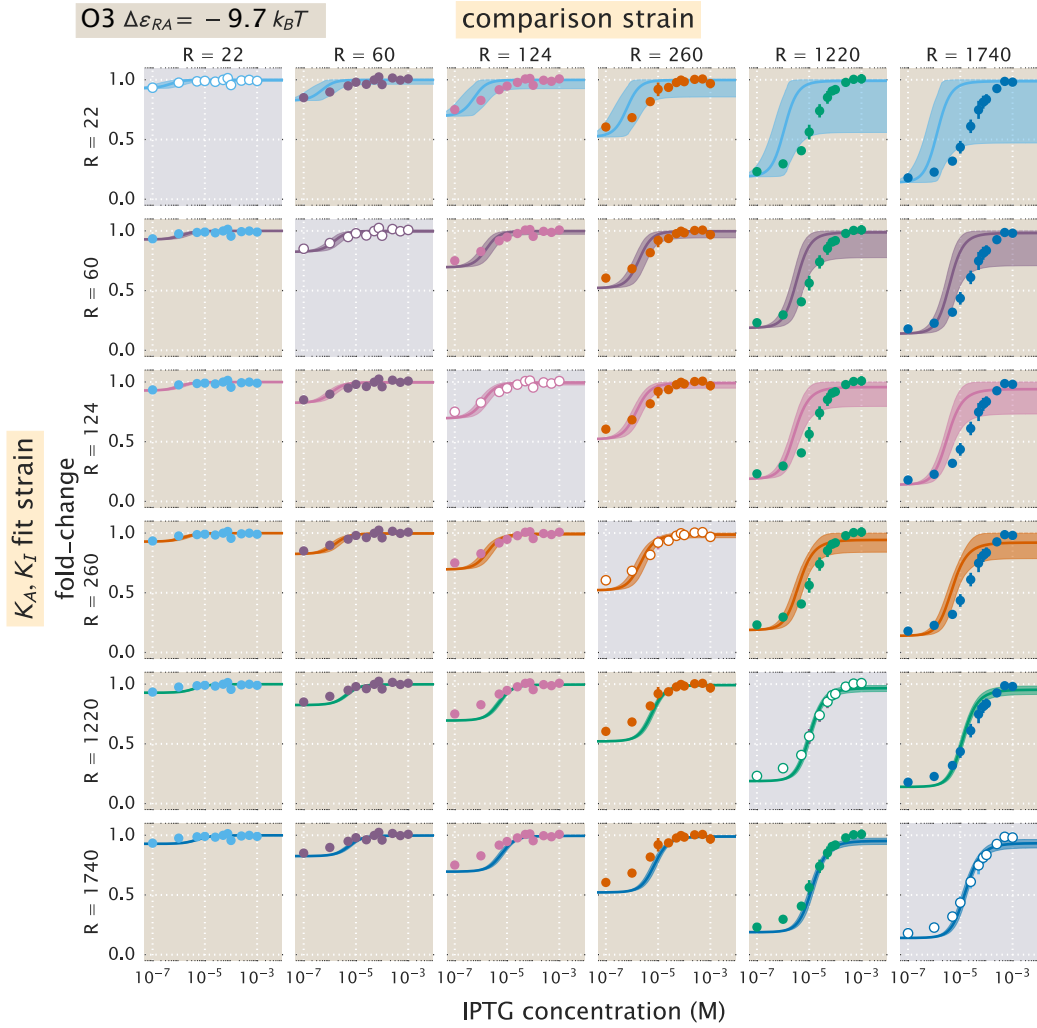
Figure S23. O3 strain fold-change predictions based on strain-specific parameter estimation of K_A and K_I. Fold-change in expression is plotted as a function of IPTG concentration for all strains containing an O3 operator. The plots and data shown are analogous to Fig. S21, but for the O3 operator. We note that when using the $R = 22$ O3 strain to predict K_A and K_I, the large uncertainty in the estimates of these parameters (see Fig. S20) leads to correspondingly wider credible regions.

J Applications to Other Regulatory Architectures

In this section, we discuss how the theoretical framework presented in this work is sufficiently general to include a variety of regulatory architectures outside of simple repression by LacI. We begin by noting that the exact same formula for fold-change given in Eq. (5) can also describe corepression. We then demonstrate how our model can be generalized to include other architectures, such as a coactivator binding to an activator to promote gene expression. In each case, we briefly describe the system and describe its corresponding theoretical description. For further details, we invite the interested reader to read references [15, 16].

J.1 Corepression

Consider a regulatory architecture where binding of a transcriptional repressor occludes the binding of RNAP to the DNA. A corepressor molecule binds to the repressor and shifts its allosteric equilibrium towards the active state in which it binds to the DNA and represses expression (in contrast, an inducer shifts the allosteric equilibrium towards the inactive state.) As in the main text, we can enumerate the states and statistical weights of the promoter and the allosteric states of the repressor. We note that these states and weights exactly match Figs. 1 and 2 and yield the same fold-change equation as Eq. (5),

$$\text{fold-change} \approx \left(1 + \frac{\left(1 + \frac{c}{K_A} \right)^n}{\left(1 + \frac{c}{K_A} \right)^n + e^{\beta \Delta \varepsilon_{AI}} \left(1 + \frac{c}{K_I} \right)^n} \frac{R}{N_{NS}} e^{-\beta \Delta \varepsilon_{RA}} \right)^{-1}, \tag{S28}$$

where c now represents the concentration of the corepressor molecule. Mathematically, the difference between these two architectures can be seen in the relative sizes of the dissociation constants K_A and K_I between the inducer and repressor in the active and inactive states, respectively and the sign of the allosteric parameter $\Delta \varepsilon_{AI}$. The corepressor is defined by $K_A < K_I$, since the corepressor favors binding to the repressor's active state; an inducer must satisfy $K_I < K_A$, as was found in the main text from the induction data (see Fig. 4).

J.2 Activation

We now turn to the case of activation. While this architecture was not studied in this work, we wish to demonstrate how the framework presented here can be extended to include transcription factors other than repressors. To that end, we consider a transcriptional activator which binds to DNA and aids in the binding of RNAP through energetic interaction term ε_{AP}. Note that in this architecture, binding of the activator does not occlude binding of the polymerase. Binding of a coactivator molecule binds shifts its allosteric equilibrium towards the active state ($K_A < K_I$), where the activator is more likely to be bound to the DNA and promote expression. Enumerating all of the states and statistical weights of this architecture and making the approximation that the promoter is weak generates a fold-change equation of the form

$$\text{fold-change} = \frac{1 + \frac{\left(1 + \frac{c}{K_A} \right)^n}{\left(1 + \frac{c}{K_A} \right)^n + e^{\beta \Delta \varepsilon_{AI}} \left(1 + \frac{c}{K_I} \right)^n} \frac{A}{N_{NS}} e^{-\beta \Delta \varepsilon_{AA}} e^{-\beta \varepsilon_{AP}}}{1 + \frac{\left(1 + \frac{c}{K_A} \right)^n}{\left(1 + \frac{c}{K_A} \right)^n + e^{\beta \Delta \varepsilon_{AI}} \left(1 + \frac{c}{K_I} \right)^n} \frac{A}{N_{NS}} e^{-\beta \Delta \varepsilon_{AA}}}, \tag{S29}$$

where A is the total number of activators per cell, c is the concentration of a coactivator molecule, $\Delta \varepsilon_{AA}$ is the binding energy of the activator to the DNA in the active allosteric state, and ε_{AP} is the interaction energy between the activator and the RNAP. Unlike in the cases of induction and corepression, the fold-change formula for activation includes terms from when the RNAP is bound by itself on the DNA as well as when both RNAP and the activator are simultaneously bound to the DNA.

As in the case of induction, the Eq. (S29) is straightforward to generalize. For example, the relative values of K_I and K_A can be switched such that $K_I < K_A$ in which the secondary molecule drives the

activator to assume the inactive state represents induction of an activator. In this regime, the sign of the allosteric parameter $\Delta\varepsilon_{AI}$ becomes negative.While these cases might be viewed as separate biological phenomena, mathematically they can all be described by the same formalism and result in the same formula.

K *E. coli* Primer and Strain List

Here we provide additional details about the genotypes of the strains used, as well as the primer sequences used to generate them. *E. coli* strains were derived from K12 MG1655. For those containing $R = 22$, we used strain HG104 which additionally has the *lacYZA* operon deleted (positions 360,483 to 365,579) but still contains the native *lacI* locus. All other strains used strain HG105, where both the *lacYZA* and *lacI* operons have both been deleted (positions 360,483 to 366,637).

All 25x+11-yfp expression constructs were integrated at the *galK* locus (between positions 1,504,078 and 1,505,112) while the 3*1x-lacI constructs were integrated at the *ybcN* locus (between positions 1,287,628 and 1,288,047). Integration was performed with λ Red recombineering [17] as described in [8] using the primers listed in Table S3. We follow the notation of Lutz and Bujard [18] for the nomenclature of the different constructs used. Specifically, the first number refers to the antibiotic resistance cassette that is present for selection (2 = kanamycin, 3 = chloramphenicol, and 4 = spectinomycin) and the second number refers to the promoter used to drive expression of either YFP or LacI (1 = $P_{LtetO-1}$, and 5 = *lacUV5*). Note that in 25x+11-yfp, x refers to the LacI operator used, which is centered at +11 (or alternatively, begins at the transcription start site). For the different LacI constructs, 3*1x-lacI, x refers to the different ribosomal binding site modifications that provide different repressor copy numbers and follows from Garcia *et al.* [8]. The asterisk refers to the presence of FLP recombinase sites flanking the chloramphenicol resistance gene that can be used to lose this resistance. However, we maintained the resistance gene in our constructs. A summary of the final genotypes of each strain is listed in Table S4. In addition each strain also contained the plasmid pZS4*1-mCherry and provided constitutive expression of the mCherry fluorescent protein. This pZS plasmid is a low copy (SC101 origin of replication) where like with 3*1x-lacI, mCherry is driven by a $P_{LtetO-1}$ promoter.

Table S3. Primers used in this work. Lower case sequences denote homology to a chromosomal locus used for integration of the construct into the *E. coli* chromosome. Uppercase sequences refer to the sequences used for PCR amplification.

Primer	Sequence	Comment
General sequencing primers:		
pZSForwSeq2	TTCCCAACCTTACCAGAGGGC	Forward primer for 3*1x-lacI
251F	CCTTTCGTCTTCACCTCGA	Forward primer for 25x+11-yfp
YFP1	ACTAGCAACACCAGAACAGCCC	Reverse primer for 3*1x-lacI and 25x+11-yfp
Integration primers:		
HG6.1 (*galK*)	gtttgcgcgcagtcagcgatatccattttcgcgaatccgg agtgtaagaaACTAGCAACACCAGAACAGCC	Reverse primer for 25x+11-yfp with homology to *galK* locus.
HG6.3 (*galK*)	ttcatattgttcagcgacagcttgctgtacggcaggcacc agctcttccgGGCTAATGCACCCAGTAAGG	Forward primer for 25x+11-yfp with homology to *galK* locus.
galK-control-upstream1	TTCATATTGTTCAGCGACAGCTTG	To check integration.
galK-control-downstream1	CTCCGCCACCGTACGTAAATT	To check integration.
HG11.1 (*ybcN*)	acctctgcggaggggaagcgtgaacctctcacaagacggc atcaaattacACTAGCAACACCAGAACAGCC	Reverse primer for 3*1x-lacI with homology to *ybcN* locus.
HG11.3 (*ybcN*)	ctgtagatgtgtccgttcatgacacgaataagcggtgtag ccattacgccGGCTAATGCACCCAGTAAGG	Forward primer for 3*1x-lacI with homology to *ybcN* locus.
ybcN-control-upstream1	AGCGTTTGACCTCTGCGGA	To check integration.
ybcN-control-downstream1	GCTCAGGTTTACGCTTACGACG	To check integration.

Table S4. *E. coli* strains used in this work. Each strain contains a unique operator-yfp construct for measurement of fluorescence and R refers to the dimer copy number as measured by Garcia *et al.* [8].

Strain	Genotype
O1, $R = 0$	HG105::galK⟨⟩25O1+11-yfp
O1, $R = 22$	HG104::galK⟨⟩25O1+11-yfp
O1, $R = 60$	HG105::galK⟨⟩25O1+11-yfp, ybcN⟨⟩3*1RBS1147-lacI
O1, $R = 124$	HG105::galK⟨⟩25O1+11-yfp, ybcN⟨⟩3*1RBS1027-lacI
O1, $R = 260$	HG105::galK⟨⟩25O1+11-yfp, ybcN⟨⟩3*1RBS446-lacI
O1, $R = 1220$	HG105::galK⟨⟩25O1+11-yfp, ybcN⟨⟩3*1RBS1-lacI
O1, $R = 1740$	HG105::galK⟨⟩25O1+11-yfp, ybcN⟨⟩3*1-lacI (RBS1L)
O2, $R = 0$	HG105::galK⟨⟩25O2+11-yfp
O2, $R = 22$	HG104::galK⟨⟩25O2+11-yfp
O2, $R = 60$	HG105::galK⟨⟩25O2+11-yfp, ybcN⟨⟩3*1RBS1147-lacI
O2, $R = 124$	HG105::galK⟨⟩25O2+11-yfp, ybcN⟨⟩3*1RBS1027-lacI
O2, $R = 260$	HG105::galK⟨⟩25O2+11-yfp, ybcN⟨⟩3*1RBS446-lacI
O2, $R = 1220$	HG105::galK⟨⟩25O2+11-yfp, ybcN⟨⟩3*1RBS1-lacI
O2, $R = 1740$	HG105::galK⟨⟩25O2+11-yfp, ybcN⟨⟩3*1-lacI (RBS1L)
O3, $R = 0$	HG105::galK⟨⟩25O3+11-yfp
O3, $R = 22$	HG104::galK⟨⟩25O3+11-yfp
O3, $R = 60$	HG105::galK⟨⟩25O3+11-yfp, ybcN⟨⟩3*1RBS1147-lacI
O3, $R = 124$	HG105::galK⟨⟩25O3+11-yfp, ybcN⟨⟩3*1RBS1027-lacI
O3, $R = 260$	HG105::galK⟨⟩25O3+11-yfp, ybcN⟨⟩3*1RBS446-lacI
O3, $R = 1220$	HG105::galK⟨⟩25O3+11-yfp, ybcN⟨⟩3*1RBS1-lacI
O3, $R = 1740$	HG105::galK⟨⟩25O3+11-yfp, ybcN⟨⟩3*1-lacI (RBS1L)
Oid, $R = 0$	HG105::galK⟨⟩25Oid+11-yfp
Oid, $R = 22$	HG104::galK⟨⟩25Oid+11-yfp
Oid, $R = 60$	HG105::galK⟨⟩25Oid+11-yfp, ybcN⟨⟩3*1RBS1147-lacI
Oid, $R = 124$	HG105::galK⟨⟩25Oid+11-yfp, ybcN⟨⟩3*1RBS1027-lacI
Oid, $R = 260$	HG105::galK⟨⟩25Oid+11-yfp, ybcN⟨⟩3*1RBS446-lacI
Oid, $R = 1220$	HG105::galK⟨⟩25Oid+11-yfp, ybcN⟨⟩3*1RBS1-lacI
Oid, $R = 1740$	HG105::galK⟨⟩25Oid+11-yfp, ybcN⟨⟩3*1-lacI (RBS1L)

References

1. Daber R, Sochor MA, Lewis M. 2011. Thermodynamic analysis of mutant lac repressors. *Journal of Molecular Biology* **409**: 76–87.

2. Daber R, Sharp K, Lewis M. 2009. One Is Not Enough. *Journal of Molecular Biology* **392**: 1133–1144.

3. Kuhlman T, Zhang Z, Saier MH, Hwa T. 2007. Combinatorial transcriptional control of the lactose operon of *Escherichia coli*. *Proceedings of the National Academy of Sciences of USA* **104**: 6043–8.

4. Setty Y, Mayo AE, Surette MG, Alon U. 2003. Detailed map of a cis-regulatory input function. *Proceedings of the National Academy of Sciences* **100**: 7702–7707.

5. Chroma Technology Corporation. 2016. Chroma spectra viewer. URL https://www.chroma.com/spectra-viewer?fluorochromes=10455.

6. Garcia HG, Lee HJ, Boedicker JQ, Phillips R. 2011. Comparison and Calibration of Different Reporters for Quantitative Analysis of Gene Expression. *Biophysical Journal* **101**: 535–544.

7. Brewster RC, Weinert FM, Garcia HG, Song D, Rydenfelt M, Phillips R. 2014. The transcription factor titration effect dictates level of gene expression. *Cell* **156**: 1312–1323.

8. Garcia HG, Phillips R. 2011. Quantitative dissection of the simple repression input-output function. *Proceedings of the National Academy of Sciences of USA* **108**: 12173–8.

9. Edelstein AD, Tsuchida MA, Amodaj N, Pinkard H, Vale RD, Stuurman N. 2014. Advanced methods of microscope control using μManager software. *Journal of Biological Methods* **1**: 10–10.

10. Marr D, Hildreth E. 1980. Theory of Edge Detection. *Proceedings of the Royal Society B: Biological Sciences* **207**: 187–217.

11. Gardino AK, Volkman BF, Cho HS, Lee SY, Wemmer DE, Kern D. 2003. The NMR Solution Structure of BeF3-Activated Spo0F Reveals the Conformational Switch in a Phosphorelay System. *Journal of Molecular Biology* **331**: 245–254.

12. Boulton S, Melacini G. 2016. Advances in NMR Methods To Map Allosteric Sites: From Models to Translation. *Chemical Reviews* **116**: 6267–6304.

13. Sivia D, Skilling J. 2006. Data analysis: a Bayesian tutorial. OUP Oxford.

14. Martins BMC, Swain PS. 2011. Trade-Offs and constraints in allosteric sensing. *PLoS Computational Biology* **7**: 1–13.

15. Marzen S, Garcia HG, Phillips R. 2013. Statistical mechanics of Monod-Wyman-Changeux (MWC) models. *Journal of Molecular Biology* **425**: 1433–1460.

16. Bintu L, Buchler NE, Garcia HG, Gerland U, Hwa T, Kondev J, Phillips R. 2005. Transcriptional regulation by the numbers: models. *Current Opinion in Genetics & Development* **15**: 116–124.

17. Sharan SK, Thomason LC, Kuznetsov SG, Court DL. 2009. Recombineering: a homologous recombination-based method of genetic engineering. *Nature Protocols* **4**: 206—223.

18. Lutz R, Bujard H. 1997. Independent and tight regulation of transcriptional units in *Escherichia coli* via the LacR/O, the TetR/O and AraC/I1-I2 regulatory elements. *Nucleic acids research* **25**: 1203–10.